# The Effect of Soluble Surfactant on the Transient Motion of a Buoyancy-Driven Bubble

by

Savaş Taşoğlu

A Thesis Submitted to the
Graduate School of Engineering
in Partial Fulfillment of the Requirements for
the Degree of

Master of Science

in

Mechanical Engineering

Koç University

July, 2008

Koç University

Graduate School of Sciences and Engineering

This is to certify that I have examined this copy of a master's thesis by

Savaş Taşoğlu

and have found that it is complete and satisfactory in all respects,
and that any and all revisions required by the final
examining committee have been made.

Committee Members:

Assoc. Prof. Metin Muradoğlu (Advisor)

Asst. Prof. Cağatay Başdoğan

Asst. Prof. Mehmet Sayar

Date: _____

*To my parents*

## ABSTRACT

In this thesis the effect of soluble surfactants on the unsteady motion and deformation of a bubble rising in an otherwise quiescent liquid contained in an axisymmetric tube is studied computationally using a finite-difference/front-tracking method. The unsteady incompressible flow equations are solved fully coupled with the evolution equations of bulk and interfacial surfactant concentrations. The surface tension is related to the interfacial surfactant concentration by a non-linear equation of state. The nearly spherical, ellipsoidal and dimpled ellipsoidal-cap regimes of bubble motion are examined. It is found that surfactant generally reduces the terminal velocity of the bubble but this reduction is most pronounced in the nearly spherical regime in which the bubble behaves like a solid sphere and its terminal velocity approaches that of an equivalent solid sphere. Effects of the elasticity number, and the bulk and interfacial Peclet numbers are examined in the spherical and ellipsoidal regimes. It is found that the surface flow and interfacial surfactant concentration profiles exhibit the formation of a stagnant-cap at the trailing end of the bubble in the ellipsoidal regime at low elasticity and high interfacial Peclet numbers. Bubble deformation is first reduced due to rigidifying effect of the surfactant but is then amplified when the elasticity number exceeds a critical value due to overall reduction in the surface tension.



**Keywords:** Bubbles, deformation, elasticity, finite-difference/front-tracking method, surfactants, two-phase flow

# ÖZETÇE

Bu tezde sonlu-farklar/arayüz-izleme metodu kullanılarak çözünür yüzey aktif maddelerin içi sıvı dolu olan kanal boyunca yükselen gaz kabarcığının zamana bağlı hareketi ve deformasyonu üzerindeki etkisi incelendi. Zamana bağlı sıkıştırılamaz akış denklemleri, arayüzde ve gaz kabarcığının dışındaki fazda yüzey aktif madde taşınım denklemleri ile bağlı şekilde çözüldü. Yüzey gerilimini yüzey aktif maddenin fonksiyonu olarak tanımlamak için, lineer olmayan bir durum denklemi kullanıldı. Küresel, ellipsoidal ve çukurlu ellipsoidal benzeri gaz kabarcığı hareket rejimleri incelendi. Sonuçlarımızda yüzey aktif maddelerin genel olarak gaz kabarcığının son hızını azalttığını fakat bu yavaşlamanın küresel gaz kabarcıklarında daha belirgin olduğunu ve bu tür gaz kabarcıklarının küresel katı cisim gibi davrandığını bulduk. Elastisite, ve yığınsal ve yüzey Peklet sayılarının etkisi küresel ve ellipsoidal rejimler için çalışıldı. Düşük elastisite ve yüksek yüzey Peklet sayılarında ellipsoidal rejimdeki gaz kabarcığının arkasında hareketsiz-kapsül oluşumu gözlendi. Kabarcık deformasyonu yüzey aktif maddenin sertleştirici etkisinden dolayı başta azaldı fakat daha sonra elastisite sayısı toplam yüzey gerilim azalmasından dolayı kritik değeri aştı ve sonuç olarak deformasyon da arttı.

**Anahtar kelimeler:** Kabarcık, deformasyon, elastisite, sonlu-farklar/arayüz-izleme metodu, yüzey aktif maddeler, çift fazlı akış

## ACKNOWLEDGMENTS

First, I would like to thank my supervisor Assoc. Prof. Metin Muradoğlu who have been a great source of inspiration and provided the right balance of suggestions, criticism, and freedom. He shared his knowledge & experience with me, paid attention to all the steps of my thesis, and provided me his recommendations that guided me.

I am grateful to members of my thesis committee for critical reading of this thesis and for their valuable comments.

Many thanks are due to my grad student friends whose friendship have made the years in Koç University a memorable time in my life.

Finally, I would like to thank my family for providing me a morale support that helps me in hard days of my research. All this would not be possible without the support of my mother Adalet Özdemir and my father Sait Taşoğlu.

## TABLE OF CONTENTS

## LIST OF FIGURES

# NOMENCLATURE

| | |
|---|---|
| FD/FT | Finite-difference/Front-tracking |
| $\mathbf{u}$ | velocity |
| $p$ | pressure |
| $\rho_o$ | density of the ambient fluid |
| $\rho_b$ | density of bubble |
| $\mu_o$ | viscosity of the ambient fluid |
| $\mu_b$ | viscosity of bubble |
| $t$ | physical time |
| $t^*$ | non-dimensional time |
| $s$ | arc length |
| $\sigma$ | surface tension |
| $\kappa$ | curvature |
| $\mathbf{x}$ | location of a front point |
| $\mathbf{x}_f$ | location of the front |
| $I$ | indicator function |
| $M_s$ | total mass of surfactant |
| $A$ | surface area |
| $\mathcal{R}$ | ideal gas constant |
| $T$ | absolute temperature |
| $\delta$ | Delta function |
| $R$ | channel radius |
| $L$ | channel length |
| $a$ | bubble radius |
| $\Gamma$ | surfactant concentration at the interface |
| $\Gamma_\infty$ | maximum surfactant concentration at the interface |

| | |
|---|---|
| $D_s$ | surface diffusion coefficient |
| $D_c$ | bulk diffusion coefficient |
| $C$ | bulk surfactant concentration |
| $C_\infty$ | bulk surfactant concentration far from the interface |
| $C_s$ | surfactant concentration in fluid immediately adjacent to the interface |
| $\sigma_s$ | surface tension of a clean interface |
| $\mathcal{L}$ | length scale |
| $\mathcal{U}$ | velocity scale |
| $\mathcal{T}$ | time scale |
| $Re$ | Reynolds number |
| $Ca$ | capillary number |
| $Pe_c$ | Peclet number based on bulk surfactant diffusivity |
| $Pe_s$ | Peclet number based on interface surfactant diffusivity |
| $k$ | dimensionless adsorption depth |
| $Bi$ | Biot number |
| $Da$ | Damkohler number |
| $Eo$ | Eötvös number |
| $Mo$ | Morton number |
| $\beta_s$ | elasticity number |
| $k_a$ | adsorption coefficient |
| $k_b$ | desorption coefficient |

# Chapter 1

# INTRODUCTION

## *1.1 Literature Review*

Surface active agents (surfactant) are either present as impurities that are difficult to remove from a system or they are added deliberately to fluid mixtures to manipulate interfacial flows. It has been well known that presence of surfactant in a fluid mixture can critically alter the motion and deformation of bubbles moving through a continuous liquid phase [1, 2]. Probably the best known example is the retardation effect of surfactant on the buoyancy-driven motion of small bubbles. Numerous experimental studies [1, 3, 4] have shown that the terminal velocity of a contaminated spherical bubble is significantly smaller than the classical Hadamard-Rybczynski prediction [5, 6] and approaches the terminal velocity of an equivalent solid sphere. The physical mechanism for this behavior was first explained consistently by Frumkin and Levich [7] by noting that the surfactant adsorbed from the bulk fluid is convected towards the back of the bubble and the resulting Marangoni stresses act to reduce the interface mobility. This reduction in surface mobility increases the drag force and thus reduces the terminal velocity [1, 2, 8].

The effect of surfactant on the rise of a single spherical bubble of various diameters has been studied experimentally by Bel Fdliha and Duineveld [9] and more recently by Zhang and Finch [10]. Bel Fdliha and Duineveld [9] measured the steady terminal rise velocity of bubble and reported a dependence on the bulk surfactant concentration. Zhang and Finch [10] measured the transient rise velocity of a spherical bubble for three different bulk surfactant concentrations. They showed that the distance to reach a steady-state gets shorter but the steady rise velocity remains the same as the bulk surfactant concentration increases. The effect of surfactant on the steady motion of a buyancy-driven bubble moving through a capillary tube with significant deformations was studied experimentally by

Almatroushi and Borhan [11]. They found that the contamination retards the motion of small bubbles due to the development of adverse Marangoni stresses whereas it enhances the mobility of large bubbles by increasing their deformability away from the tube wall. They also found that the steady rise velocity of small bubbles is unaffected while the mobility of large bubbles is slightly increased as the bulk concentration is increased.

Due to complexity of the boundary conditions at deforming interface, the problem has been usually studied using the simplifying assumptions of a non-deforming spherical bubble and the creeping flow limit. However, even in this limit, no complete analytical solution has been achieved. Frumkin and Levich [7] proposed a uniformly retarded interfacial velocity model but this model has proved to be insufficient to fully explain experimental observations [3, 12]. Savic [13] suggested the stagnant-cap model based on his own experimental observations. The stagnant-cap regime has been then studied extensively by several authors including Griffith [14], Harper [15]-[18], Davis and Acrivos [19], Holbrook and Levan [20, 21], Sadhal and Johnson [22], and He et al. [23]. They all assumed creeping flow equations and computed the drag force as a function of cap angle for a buoyancy-driven motion of a spherical bubble. In this regard, Harper [15]-[18] has made outstanding theoretical contributions to the problem and further studied diffusion boundary-layer of surfactant around a stagnant-cap bubble, allowing both for adsorption and diffusion [18]. Bel Fdliha and Duineveld [9] extended the method developed by Sadhal and Johnson [22] to finite Reynolds numbers by solving the momentum equations around a spherical bubble with the stagnant-cap boundary conditions. Leppinen et al. [24, 25] and McLaughlin [26] took a step forward and considered deforming interfaces but they both ignored the surfactant solubility. On the other hand, Cuenot et al. [27] considered the surfactant solubility, but ignored bubble deformation and demonstrated the validity of stagnant-cap model to describe flow around a bubble slightly contaminated by a soluble surfactant. They also found that a simple relation between cap angle and bulk concentration cannot generally be obtained since diffusion from the bulk plays a significant role. Takemura [28] used a similar method to study the effects of Reynolds number and bulk surfactant concentration on the adsorption and the terminal velocity of a single bubble in an unbounded domain. They found that surfactant adsorption at the front of the bubble with respect to rise direction is lower than that at the back, and this difference increases with increasing Reynolds number and/or decreasing bulk surfactant

concentration. Wang et al. [29] studied theoretically the slow motion of contaminated gas bubbles rising steadily in an unbounded liquid in creeping flow and showed that the mobility of surfactant-retarded bubble interface can be increased by raising the bulk surfactant concentration. Recently, Palaparthi et al. [30] studied theoretically and experimentally the effects of soluble surfactants on the motion of a spherical bubble in the stagnant-cap regime. They showed that very small bulk concentration can immobilize the entire bubble surface.

Full Navier-Stokes simulations with finite-rate mass exchange between the interface and bulk fluid have been recently performed by Sugiyama et al. [31], Liao and McLaughlin [32] and Li and Mao [33]. Sugiyama et al. [31] extended the study by Cuenot et al. [27] and allowed the bubble deformation. They solved the full Navier-Stokes equations coupled with an equation for the surfactant concentration on a body-fitted orthogonal grid and studied the effect of soluble surfactants on the motion of a deformable bubble in an unbounded domain. Liao and McLaughlin [32] studied the effects of soluble surfactant on unsteady motion of a single bubble rising in an unbounded water reservoir. They used a vorticity-stream function formulation with an adaptive body-fitted grid similar to the method developed by Ryskin and Leal [34]. They reported the time evolution of bubble rise velocity as a function of bulk surfactant concentration and surfactant solubility. Li and Mao [33] also used a body-fitted grid method and simulated the steady axisymmetrical motion of a single drop in an unbounded domain at moderate Reynolds numbers. They found that drag coefficient is significantly influenced by a minute amount of the surfactant, and the flow structure is sensitive to the bulk surfactant concentration.

### *1.2 Contributions Made in this Work*

The common deficiencies of the previous full Navier-Stokes simulations can be summarized as follows:

1. The wall effects are totally ignored and the bubble is assumed to be rising in an infinite domain. In many applications, the bubble moves through a finite size channel and channel walls have significant influence on motion and deformation of the bubble [1, 11].

2. The terminal velocity of bubble is fixed throughout the simulation, which is impossible

to achieve experimentally. Only exception is that Liao and McLaughlin [32] allowed bubble to rise from rest but Liao et al. [35] reported significant numerical inaccuracies making their results unreliable.

The aim of this thesis is first to remedy these deficiencies and then investigate unsteady motion and deformation of a contaminated gas bubble rising in an otherwise quiescent liquid contained in an axisymmetrical capillary tube. For this purpose, the incompressible Navier-Stokes equations are solved fully coupled with the evolution equations of the interfacial and bulk surfactant concentrations using a finite-difference/front-tracking method developed by Muradoglu and Tryggvason [36]. A non-linear equation of state based on the Langmuir adsorption [37] is used to relate the surface tension coefficient to the interfacial surfactant concentration. A nearly spherical, ellipsoidal, and dimpled ellipsoidal-cap regimes are studied. The effect of tube wall on the terminal velocity of clean and contaminated bubble in the nearly spherical regime is investigated and results are compared with the experimental correlations collected by Clift et al. [1]. Extensive computations are performed to show the time evolution of interfacial and bulk surfactant concentrations, the effects of governing non-dimensional numbers such as elasticity number, Peclet number based on bulk surfactant diffusivity, Peclet number based on interfacial surfactant diffusivity, Damkohler number and Eötvös number on the terminal velocity and on the overall flow structure.

# Chapter 2

# MATHEMATICAL FORMULATION

Consider the axisymmetrical motion and deformation of a viscous bubble moving in a circular tube as sketched in Fig. 2.1. The flow equations are described here in the context of the finite-difference/front-tracking (FD/FT) method. The fluid motion is assumed to be governed by the incompressible Navier-Stokes equations and we solve for the flow everywhere, both inside and outside of the bubble. Following Unverdi and Tryggvason [38], a single set of governing equations can be written for the whole computational domain as long as the jump in material properties such as density, viscosity and molecular diffusion coefficient is correctly accounted for and surface tension is included.

The Navier-Stokes equations in conservative form are given by

$$\frac{\partial \rho \mathbf{u}}{\partial t} + \nabla \cdot (\rho \mathbf{u}\mathbf{u}) = -\nabla p + \nabla \cdot \mu(\nabla \mathbf{u} + \nabla \mathbf{u}^T) + \int_A \sigma(\Gamma)\kappa \mathbf{n}\delta(\mathbf{x} - \mathbf{x}_f)dA, \tag{2.1}$$

where $\mathbf{u}$ is the velocity, $p$ is the pressure, and $\rho$ and $\mu$ are the discontinuous density and viscosity fields, respectively. The effects of surface tension is included as a body force in the last term on the right hand side, where $\sigma$ is the surface tension that is function of the surfactant concentration $\Gamma$ at the interface, $\kappa$ is twice the mean curvature, and $\mathbf{n}$ is a unit vector normal to the interface. The surface tension acts only on the interface as indicated by the three-dimensional delta function $\delta$ whose arguments $\mathbf{x}$ and $\mathbf{x}_f$ are the point at which the equation is evaluated and a point at the interface, respectively.

The Navier-Stokes equations are supplemented by the incompressibility condition:

$$\nabla \cdot \mathbf{u} = 0. \tag{2.2}$$

We also assume that the material properties remain constant following a fluid particle, i.e.,

$$\frac{D\rho}{Dt} = 0; \quad \frac{D\mu}{Dt} = 0, \tag{2.3}$$

where $D/Dt$ is the material derivative. The density and viscosity vary discontinuously

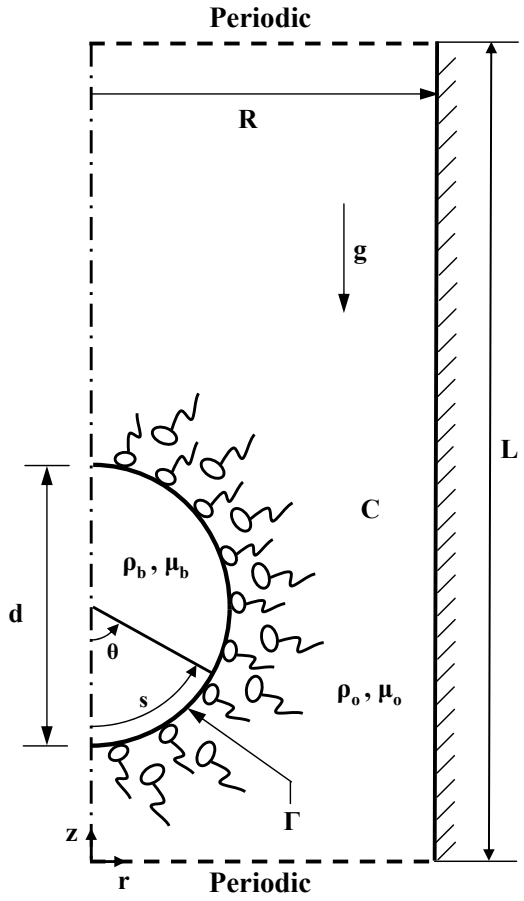


Figure 2.1: Schematic illustration of the computational setup for a buoyancy-driven bubble rising in an axisymmetrical channel with soluble surfactant.

across the fluid interface and are given by

$$\begin{aligned} \rho &= \rho_d I(r,z,t) + \rho_o(1 - I(r,z,t)), \\ \mu &= \mu_d I(r,z,t) + \mu_o(1 - I(r,z,t)), \end{aligned} \tag{2.4}$$

where the subscripts "$d$" and "$o$" denote the properties of the bubble and ambient fluid, respectively, and $I(r,z,t)$ is the indicator function defined as

$$I(r,z,t) = \begin{cases} 1 & \text{in bubble fluid,} \\ 0 & \text{in bulk fluid.} \end{cases} \tag{2.5}$$

Concentration of surfactant on the interface, $\Gamma$, is defined as

$$\Gamma = \frac{M_s}{A}, \tag{2.6}$$

where $M_s$ is the total mass of surfactant and $A$ is the surface area. The surface tension decreases proportional to the surfactant concentration at the interface according to the equation of state derived from Langmuir adsorption [37]

$$\sigma = \sigma_s + \mathcal{R}T\Gamma_\infty \ln(1 - \frac{\Gamma}{\Gamma_\infty}), \tag{2.7}$$

where $\mathcal{R}$ is the ideal gas constant, $T$ is the absolute temperature, $\sigma_s$ is the surface tension of clean interface and $\Gamma_\infty$ is the maximum packing concentration. Equation (2.7) can also be written as

$$\sigma = \sigma_s \left[1 + \beta_s \ln(1 - \frac{\Gamma}{\Gamma_\infty})\right], \tag{2.8}$$

where $\beta_s = \frac{\mathcal{R}T\Gamma_\infty}{\sigma_s}$ is the elasticity number. In the present study, Eq. (2.8) is slightly modified to avoid negative values of the surface tension as

$$\sigma = \sigma_s \left[\max\left(\epsilon_\sigma, 1 + \beta_s \ln(1 - \frac{\Gamma}{\Gamma_\infty})\right)\right], \tag{2.9}$$

where $\epsilon_\sigma$ is taken as 0.05 in the present study. The surfactant concentration $\Gamma$ evolves by [40]

$$\frac{\partial \Gamma}{\partial t} + \nabla_s \cdot (\Gamma \mathbf{U}_s) = D_s \nabla_s^2 \Gamma + \dot{S}_\Gamma, \tag{2.10}$$

where the gradient operator along the interface is defined as

$$\nabla_s = \nabla - \mathbf{n}(\mathbf{n} \cdot \nabla). \tag{2.11}$$

In Eq. (2.10), $\mathbf{U}_s$ is the tangential velocity on the interface, $D_s$ is the diffusion coefficient along the interface and $\dot{S}_\Gamma$ is the source term given by

$$\dot{S}_\Gamma = k_a C_s(\Gamma_\infty - \Gamma) - k_b\Gamma, \tag{2.12}$$

where $k_a$ and $k_b$ are adsorption and desorption coefficients, respectively, and $C_s$ is the concentration of surfactant in fluid immediately adjacent to the interface. The bulk surfactant concentration $C$ is governed by the advection-diffusion equation in the form

$$\frac{\partial C}{\partial t} + \nabla \cdot (C\mathbf{u}) = \nabla \cdot (D_{co}\nabla C)\,, \tag{2.13}$$

where the coefficient $D_{co}$ is related to the molecular diffusion coefficient $D_c$ and the indicator function $I$ as

$$D_{co} = D_c(1 - I(r, z, t)). \tag{2.14}$$

By integrating Eq. (2.10) across the interface, we find that the source term is related to the bulk concentration by [41],

$$\dot{S}_\Gamma = -D_{co}\left(\mathbf{n} \cdot \nabla C|_{interface}\right). \tag{2.15}$$

In the present method, the boundary condition at the interface given by Eq. (2.15) is first converted into a source term in a conservative manner following the same philosophy as for the immersed boundary method [43]. We assume that all the mass transfer between the interface and bulk takes place in a thin *adsorption* layer adjacent to the interface as sketched in Fig. 2.2a so that the total amount of mass adsorbed on the interface is distributed over the adsorption layer and added to the bulk concentration evolution equation as a negative source term in a conservative manner.

Equation (2.13) thus becomes

$$\frac{\partial C}{\partial t} + \nabla \cdot (C\mathbf{u}) = \nabla \cdot (D_{co}\nabla C) + \dot{S}_C, \tag{2.16}$$

where $\dot{S}_C$ is the source term evaluated at the interface and distributed onto the adsorption layer in a conservative manner as discussed in Section 3.3. With this formulation, all the mass of the bulk surfactant to be adsorbed by the interface has been already consumed in the adsorption layer before the interface so the boundary condition at the interface simplifies to be $\mathbf{n} \cdot \nabla C|_{interface} = 0$.

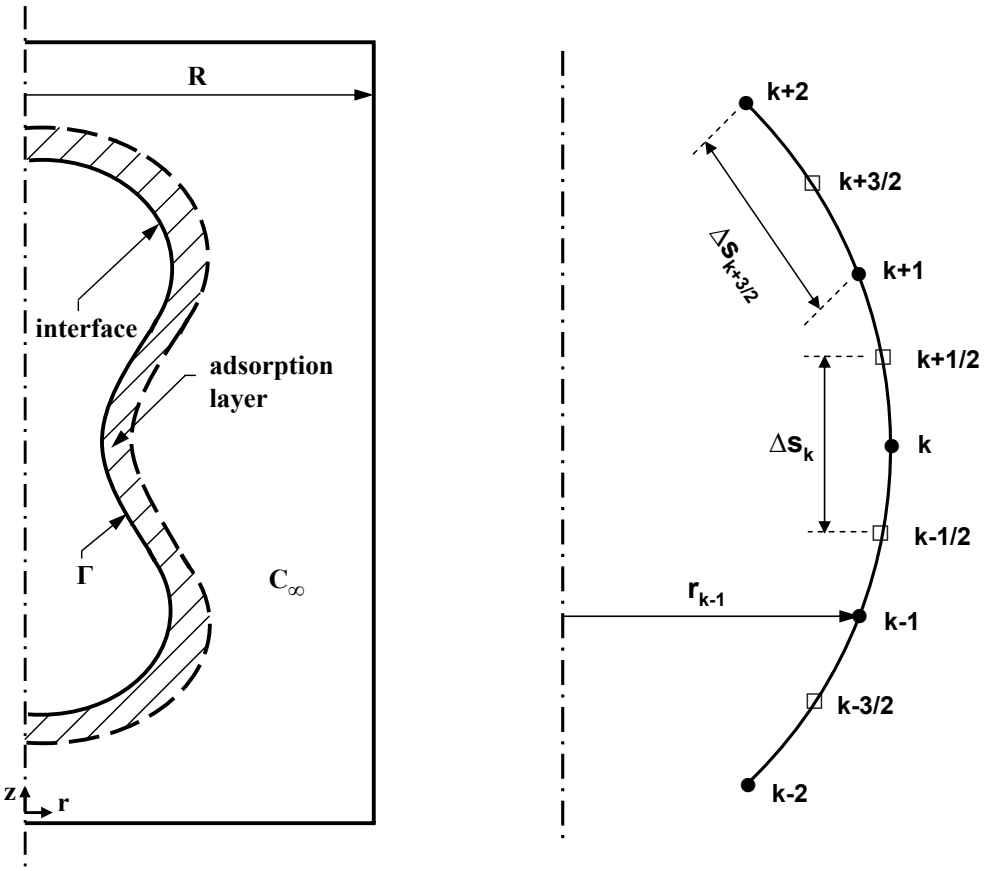


(a) (b)

Figure 2.2: (a) Schematic illustration of the adsorption layer. (b) Sketch for the spatial discretization of the surfactant concentration evolution equation on the interface. The open symbols represent the location of Lagrangian marker points while the filled symbols represent the front element centroids.

The governing equations are solved in their dimensional forms but the results are expressed in terms of relevant nondimensional quantities. Let $\mathcal{L}$ and $\mathcal{U}$ be appropriately defined length and velocity scales, respectively, and $\mathcal{T} = \mathcal{L}/\mathcal{U}$ be the time scale, then governing nondimensional numbers can be summarized as

$$\begin{aligned} Re &= \frac{\rho_o \mathcal{U}\mathcal{L}}{\mu_o}; \quad Ca = \frac{\mu_o \mathcal{U}}{\sigma_s}; \quad Pe_c = \frac{\mathcal{U}\mathcal{L}}{D_c}; \quad Pe_s = \frac{\mathcal{U}\mathcal{L}}{D_s}; \quad \frac{\rho_d}{\rho_o}; \quad \frac{\mu_d}{\mu_o}; \\ k &= \frac{k_a C_\infty}{k_b}; \quad Bi = \frac{k_b \mathcal{L}}{\mathcal{U}}; \quad Da = \frac{\Gamma_\infty}{\mathcal{L} C_\infty}, \beta_s = \frac{\mathcal{R}T\Gamma_\infty}{\sigma_s}, \end{aligned} \tag{2.17}$$

where $Re$, $Ca$, $Pe_c$, $Pe_s$, $k$, $Bi$, $Da$ and $\beta_s$ are the Reynolds number, the capillary number, the Peclet number based on bulk surfactant diffusivity, the Peclet number based on interface surfactant diffusivity, the dimensionless adsorption depth, Biot number, Damkohler number and the elasticity number, respectively.

# Chapter 3

# NUMERICAL SOLUTION PROCEDURE

The flow equations are solved together with the bulk and interface surfactant concentration evolution equations using a FD/FT method [46, 38]. In this method, the interface is represented by connected Lagrangian marker points moving with the local flow velocity interpolated from the neighboring stationary regular Cartesian Eulerian grid as sketched in Fig. 3.1.

A piece of the interface between two neighboring marker points is called a front element. The material properties inside and outside of the bubble are set based on the indicator function defined by Eq. (2.5). The indicator function is computed on the Eulerian grid using the same procedure as described by Tryggvason et al. [46]. The method is briefly outlined here. The discontinuity is spread onto the grid points adjacent to the interface resulting in the gradient field

$$\mathbf{G}(\mathbf{x}) \quad = \quad \nabla I = \int_A \mathbf{n}\delta(\mathbf{x} - \mathbf{x}_f)dA, \tag{3.1}$$

which is zero everywhere except at the interface. Note that the vector field $\mathbf{G}$ is also utilized to enforce the no mass flux boundary condition for the bulk surfactant concentration at the interface as will be discussed in Section 3.3. Taking the divergence of both sides of Eq. (3.1) yields

$$\nabla^2 I = \nabla \cdot \mathbf{G}, \tag{3.2}$$

which is a separable Poisson equation and can be solved efficiently in the vicinity of the bubble. The delta function appearing in Eq. (3.1) is approximated by Peskin's cosine distribution function [43]. The same function is also used to distribute the surface tension forces computed at the center of front elements over the neighboring grid points and also to interpolate the velocity vector from the Eulerian grid onto the marker points. This distribution function is sketched in Fig. 3.2a.

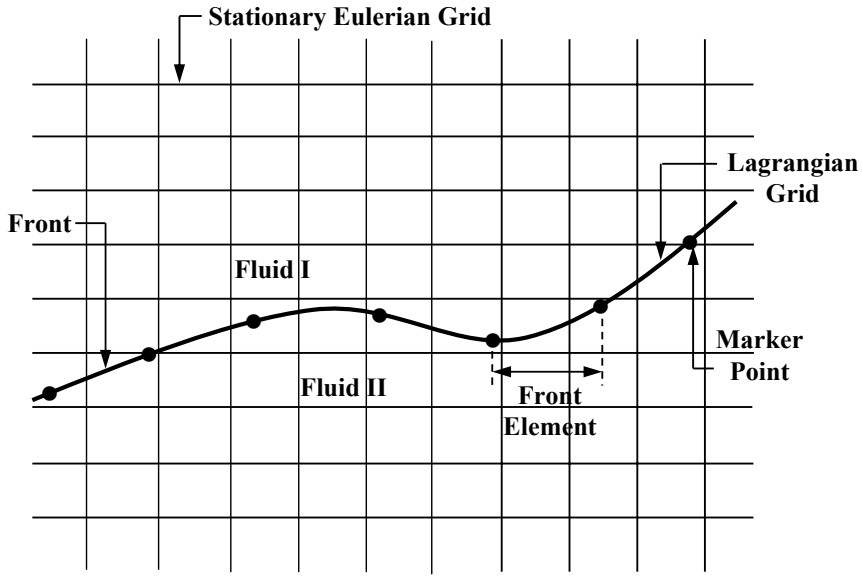


Figure 3.1: Schematic illustration of the computational grids employed.

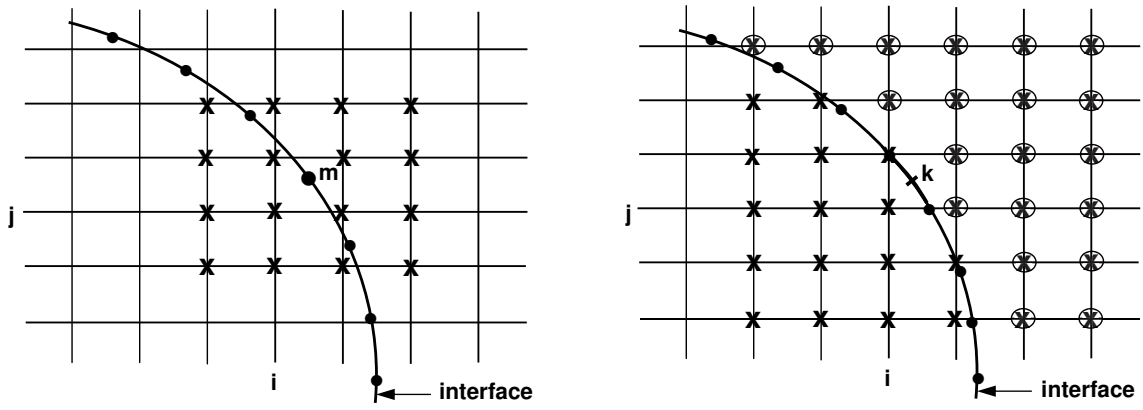


(a) (b)

Figure 3.2: Sketch for interpolation schemes. (a) Velocity is interpolated onto the location of $m^{\text{th}}$ marker point from 16 neighboring Eulerian grid nodes. Similarly, the surface tension force computed at the front element centroid is distributed onto 16 neighboring Eulerian grid nodes. (b) The bulk surfactant concentration is interpolated from the Eulerian grid nodes outside of the bubble onto $k^{\text{th}}$ front element and the source term computed on the front element is distributed onto the same Eulerian grid nodes.

In Eq. (3.2), the divergence operator is approximated using second order central differences and then the Poisson equation is solved using a fast Poisson solver [44]. The computed indicator function is constant in each material region but with a finite-thickness transition zone at the interface. Therefore the transition region approximates a two-dimensional Heaviside function.

The Lagrangian grid is also used to compute the surface tension forces at the interface which are then distributed over the neighboring Eulerian grid cells as body forces in a conservative manner [46, 38] using Peskin's distribution function. Since the FD/FT method has been described in details by Unverdi and Tryggvason [38] and by Tryggvason et al. [46] for surfactant-free flows, the basic flow solver is discussed only briefly here for completeness and emphasis is placed on the solution of the bulk and interfacial surfactant concentration evolution equations.

### *3.1 Flow Solver*

The flow equations (Eqs. (2.1) and (2.2)) are solved on a stationary staggered Eulerian grid. The spatial derivatives are approximated using second order central finite-differences for all field quantities. The time integration is achieved using a projection method. Following Unverdi and Tryggvason [38], Eqs. (2.1) and (2.2) are written in the form

$$\frac{\rho^{n+1}\mathbf{u}^{n+1} - \rho^n \mathbf{u}^n}{\Delta t} = \mathbf{A}^n - \nabla p, \tag{3.3}$$

$$\nabla \cdot \mathbf{u}^{n+1} = 0, \tag{3.4}$$

where $\mathbf{A}$ is the advective, diffusive and body force terms in Eq. (2.1). Then the above equation is decomposed as

$$\frac{\rho^{n+1}\mathbf{u}^{*} - \rho^n \mathbf{u}^n}{\Delta t} = \mathbf{A}^n, \tag{3.5}$$

$$\frac{\rho^{n+1}\mathbf{u}^{n+1} - \rho^{n+1} \mathbf{u}^{*}}{\Delta t} = -\nabla p, \tag{3.6}$$

where $\mathbf{u}^*$ is a provisional velocity ignoring the effect of the pressure. Next the unprojected velocity field is computed from Eq. (3.6) and then the pressure field is computed as follows: taking the divergence of Eq. (3.6) and using the incompressibility condition given by Eq. (3.4), we obtain a non-separable Poisson equation for pressure in the form

$$\nabla \cdot \frac{1}{\rho^{n+1}} \nabla p = -\frac{1}{\Delta t} \nabla \cdot \mathbf{u}^{*}, \tag{3.7}$$

which is solved on the Eulerian grid using a multigrid method as described by Tryggvason et al. [46]. Finally the velocity field at the new time level is computed as

$$\mathbf{u}^{n+1} = \mathbf{u}^* - \frac{\Delta t}{\rho^{n+1}} \nabla p. \tag{3.8}$$

In the present study we use a first order explicit time integration method for the time derivatives as described above. However, second order time integration can be easily achieved by a predictor corrector method as discussed by Tryggvason et al. [46].

### *3.2 Surfactant Concentration at Interface*

The evolution equation of the surfactant concentration at the interface is solved on the Lagrangian grid. From Eqs. (2.10) and (2.11), we obtain

$$\frac{\partial \Gamma}{\partial t} + \nabla \cdot (\Gamma \mathbf{U}_s) - \Gamma \mathbf{n} \cdot \nabla \mathbf{U}_s \cdot \mathbf{n} = D_s \nabla_s^2 \Gamma + \dot{S}_\Gamma. \tag{3.9}$$

On the other hand, the area of an element of the interface evolves by [45]

$$\frac{DA}{Dt} = \frac{\partial A}{\partial t} + \mathbf{U}_s \cdot \nabla A = -A(\mathbf{n} \cdot \nabla \mathbf{u} \cdot \mathbf{n}). \tag{3.10}$$

Combining Eqs. (3.9) and (3.10), one obtains

$$\frac{d\Gamma A}{dt} = A D_s \nabla_s^2 \Gamma + A \dot{S}_\Gamma. \tag{3.11}$$

For an axisymmetric problem, Eq. (3.11) can be written as

$$\frac{d\Gamma A}{dt} = A \left( D_s \frac{1}{r} \frac{\partial}{\partial s} (r \frac{\partial \Gamma}{\partial s}) + \dot{S}_\Gamma \right), \tag{3.12}$$

where $s$ is the arc length along the interface and $r$ is the radial coordinate in cylindrical coordinates. Equation (3.12) can be expressed in compact form as

$$\frac{d\Gamma A}{dt} = A f(\Gamma, t), \tag{3.13}$$

where $f$ is given by

$$f(\Gamma, t) = D_s \frac{1}{r} \frac{\partial}{\partial s} (r \frac{\partial \Gamma}{\partial s}) + \dot{S}_\Gamma. \tag{3.14}$$

Referring to the sketch in Fig. 2.2b, the right hand side of Eq. (3.12) is discretized using central differences as,

$$[Af]_k \cong \frac{A_k}{r_k} D_s [\frac{r_{k+\frac{1}{2}} \frac{\Gamma_{k+1} - \Gamma_k}{s_{k+1} - s_k} - r_{k-\frac{1}{2}} \frac{\Gamma_k - \Gamma_{k-1}}{s_k - s_{k-1}}}{s_{k+\frac{1}{2}} - s_{k-\frac{1}{2}}}] + A_k \dot{S}_{\Gamma_k}, \tag{3.15}$$

where $k$ denotes the $k^{th}$ front element whose surface area is approximated as $A_k \cong \frac{1}{2}(r_{k+\frac{1}{2}} + r_{k-\frac{1}{2}})\Delta s_k$. The time-integration is performed using a simple explicit Euler method, i.e.,

$$\Gamma^{n+1} = \frac{1}{A^{n+1}} \left[\Gamma^n A^n + \Delta t A^n f(\Gamma^n, t_n)\right]. \tag{3.16}$$

### *3.3 Bulk Surfactant Concentration*

The bulk surfactant concentration equation is solved on the staggered Eulerian grid. The bulk surfactant concentration is located at the pressure nodes. The spatial derivatives are approximated using second order central differences and time integration is performed using a first order explicit Euler method. The source term is first computed on the interface and is then distributed over the adsorption layer in a conservative manner. For this purpose, the distribution algorithm is slightly modified as follows: The source term $\dot{S}_{C_{i,j}}$ at grid point $(i, j)$ is approximated as

$$\dot{S}_{C_{i,j}} = -\sum_k \omega_{i,j}^k \dot{S}_{\Gamma_k} \frac{r_k \Delta l_k}{r_{i,j} h^2}, \tag{3.17}$$

where $\dot{S}_{\Gamma_k}$ is the source term evaluated at the center of the $k^{\text{th}}$ element, $r_k$ and $\Delta l_k$ are the radial coordinate of the center and the arc length of the $k^{\text{th}}$ element, $r_{i,j}$ is the radial coordinate of the grid node $(i, j)$, $h$ is the grid spacing and $\omega_{i,j}^k$ is the weight of grid point $(i, j)$, respectively. The weight must satisfy the consistency condition

$$\sum_i \sum_j \omega_{i,j}^k = 1, \tag{3.18}$$

in order to conserve the total source strength in going from the interface to the grid. The weight for the grid point $(i, j)$, for smoothing from the center of the $k^{\text{th}}$ element $(r_f^k, z_f^k)$, can be written as

$$\omega_{i,j}^k = \frac{\tilde{\omega}_{i,j}^k}{\sum_i \sum_j \tilde{\omega}_{i,j}^k}, \tag{3.19}$$

where the non-normalized weight function is defined as

$$\tilde{\omega}_{i,j}^k = d_c(r_f^k - ih) d_c(z_f^k - jh). \tag{3.20}$$

In Eq. (3.20), the distribution function $d_c$ is a slightly modified version of the Peskin's cosine distribution defined as

$$d_c(x) = \begin{cases} \frac{1}{W}\left(1 + \cos(\frac{\pi x}{W})\right) & \text{if } |x| < W \text{ and } I < 0.5 \\ 0, & \text{otherwise,} \end{cases} \tag{3.21}$$

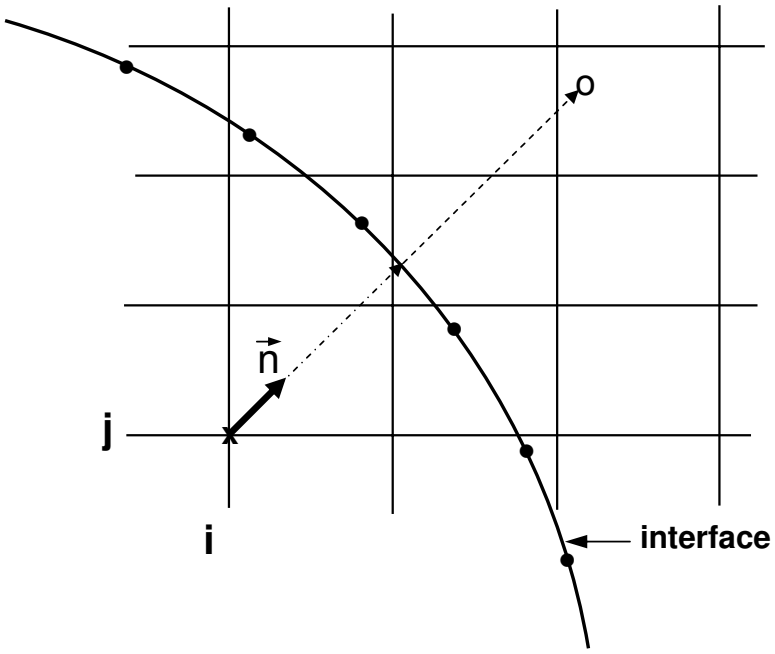


Figure 3.3: Treatment of boundary condition for the bulk concentration at the interface.

where $W$ is the width of the "adsorption" layer, taken as $W = 2h$ in the present study ($h = \Delta x$ is the grid size). Note that we have also tested a wider layer, i.e., $W = 3h$ and found that the results are not very sensitive to the width. As can be seen in Eq. (3.21), the source term is distributed only outside of the bubble region, i.e., $I(r, z, t) \leq 0.5$, which is illustrated schematically in Fig. 3.2b.

As mentioned before, in the present method, the mass exchange between the bulk fluid and the interface occurs in an *"adsorption"* layer (see Fig. 2.2a) so that the proper boundary condition for the bulk concentration at the interface becomes $\mathbf{n} \cdot \nabla C_{interface} = 0$. This condition is imposed approximately as follows: Referring to the sketch in Fig. 3.3, the no mass flux across the interface is imposed approximately by setting the bulk concentration at grid points inside the bubble, i.e., at point $(i, j)$ in the figure, to the bulk concentration at the point of reflection with respect to the interface, i.e., at point "$o$" in the figure.

The bulk concentration at the reflection point is approximated using a bilinear interpolation. In the implementation, this is done only for the grid points near the interface. For this purpose, the normal vectors that are already computed at the interface and distributed over

the grid points in the vicinity of the interface during the process of computing the indicator function [46] are utilized. First the intersection point at the interface in the direction of the normal vector is computed and then the reflection point "*o*" is computed as shown in the figure. It is found that this procedure is robust and computationally very efficient [36].

### *3.4 Overall Solution Procedure*

The finite-difference and front-tracking methods are combined as follows. In advancing the solutions from time step $n$ to step $n+1$, first the unprojected velocity field is computed from Eq. (3.6) and then the marker points are moved for a single time step by

$$\mathbf{X}_p^{n+1} = \mathbf{X}_p^n + \Delta t \mathbf{V}_p^n, \tag{3.22}$$

where $\mathbf{X}_p$ and $\mathbf{V}_p$ are the positions of the front marker points and the velocity interpolated from the neighboring Eulerian grid nodes onto the front location $\mathbf{X}_p$ using the Peskin's distribution, respectively. Next the bulk and interface surfactant concentrations are advanced for a single time step as explained above. Then the material properties are evaluated based on the new locations of the marker points as

$$\rho^{n+1} = \rho(\mathbf{X}_p^{n+1}), \quad \mu^{n+1} = \mu(\mathbf{X}_p^{n+1}), \quad \sigma^{n+1} = \sigma(\Gamma^{n+1}). \tag{3.23}$$

Finally the projected velocity field is computed from Eq. (3.6). Note that the Lagrangian grid is restructured at every time step by deleting front elements that are smaller than a prespecified lower limit and splitting front elements that are larger than a a prespecified upper limit in the same way as described by Tryggvason et al. [46] in order to keep the front element sizes nearly uniform and comparable to the Eulerian grid size. Restructuring the Lagrangian grid is of crucial importance since it avoids unresolved wiggles due to small elements and lack of resolution due to large elements. Note that the restructuring of the Lagrangian grid is performed such that the mass conservation is strictly satisfied for the surfactant at the interface. The details of the numerical method can be found in Muradoglu and Tryggvason [36].

# Chapter 4

# RESULTS AND DISCUSSION

We consider a straight cylindrical capillary tube of radius $R$ and assume that flow is axisymmetric. The physical problem and computational setup are sketched in Fig. 2.1. The computational domain is $R$ in radial direction and $L$ in the axial direction. Periodic boundary conditions are applied in the axial direction. Symmetry and no-slip boundary conditions are utilized at the centerline and at the wall of the tube, respectively. The bubble is initially located at the channel centerline close to south boundary. The interface is initially clean and the surfactant concentration is uniform in the bulk fluid at $C = C_\infty$. The bubble rises in the tube solely due to density difference between the bubble and the ambient fluids.

Besides the non-dimensional numbers given by Eq. (2.17), there are four additional independent parameters for this problem: the Eötvös number $Eo = \Delta\rho g d^2/\sigma_s$, the Morton number $Mo = \Delta\rho g \mu_o^4/\rho_o^2\sigma^3$, the non-dimensional channel diameter $D/d$ and the non-dimensional channel length $L/d$. The length and velocity scales are taken as $\mathcal{L} = d/2$ and $\mathcal{U} = V_{HR}$, respectively, where $V_{HR}$ is the terminal velocity given by Hadamard-Rybczynski solution [1] for a spherical bubble moving in an infinite domain, i.e.,

$$V_{HR} = \frac{2}{3}\frac{g a^2 \Delta\rho}{\mu_o}\frac{\mu_o + \mu_b}{2\mu_o + 3\mu_b}, \tag{4.1}$$

where $a$ is the bubble radius. The time scale is then defined as $\mathcal{T} = \mathcal{L}/\mathcal{U}$. The parameters $Pe_c$, $Pe_s$, $Bi$ and $Da$ are defined based on these scales. However, non-dimensional time ($t^*$) and Reynolds number ($Re$) are defined using the actual bubble terminal velocity ($V_b$) as the velocity scale and $\sqrt{d/g}$ as the time scale in order to facilitate direct comparison of the computational results with the available experimental data.

## *4.1 Spherical Case*

The Eötvös and Morton numbers are chosen as $Eo = 1$ and $Mo = 0.1$ for which a clean bubble moves slowly with a nearly spherical shape. The steady Reynolds number based on

the bubble terminal velocity in an unbounded domain is 0.26, which is well within the validity of the experimental correlations collected by Clift et al. [1] for clean and contaminated bubbles. Note that this case is referred as "spherical bubble" in this thesis.

### *4.1.1 The effect of the channel diameter*

First, we study the effects of surfactant on the terminal velocity of a nearly spherical bubble moving slowly in an axisymmetrical channel of various diameters. For this purpose, computations are performed for a clean and a contaminated bubbles moving in a channel with the diameters ranging between $D = 1.6d$ and $D = 15d$. Computations are performed by keeping the non-dimensional parameters constant at $L/d = 20$, $\rho_b/\rho_o = 0.1$, $\mu_b/\mu_o = 0.025$, $Pe_c = 10$, $Pe_s = 100$, $k = 1$, $Da = 10$, $Bi = 20$ and $\beta_s = 0.5$.

The grid convergence of the present finite-difference/front-tracking method has been examined [36] and it was demonstrated that it is sufficient to resolve the bubble with about 40 grid points in axial direction to reduce the spatial error below 5% for such problems. Therefore, a similar grid convergence study is not repeated here and computational grids are selected such that the bubble is resolved by about 40 grid points in the axial direction in all results presented in this thesis unless specified otherwise.

The Reynolds number is plotted in Fig. 4.1a as a function of non-dimensional time for the clean and contaminated bubbles moving in a channel with $D/d = 1.6, 2.5, 5.0, 7.5, 10.0$ and 15.0. The retardation effect of the surfactant is clearly seen in this figure, i.e., in the clean case, the bubble continuously accelerates and reaches a steady Reynolds number (or terminal velocity) while, in the contaminated case, the bubble first accelerates, reaches a peak velocity but then decelerates as the surfactant accumulates at the interface and finally reaches a steady Reynolds number. The computed steady Reynolds number is plotted in Fig. 4.1b as a function of the channel confinement ($D/d$) and compared with the available experimental data collected by Clift et al. [1] both for the clean and contaminated cases. Note that, in the contaminated bubble case, the computational results are compared with the experimental correlation obtained for an equivalent solid sphere to show the rigidifying effect of the surfactant. The computational results are shown by connected symbols while the experimental data are shown by solid and dashed lines for the fluid and solid spheres, respectively. As seen in Fig. 4.1, there is a good agreement between the computational

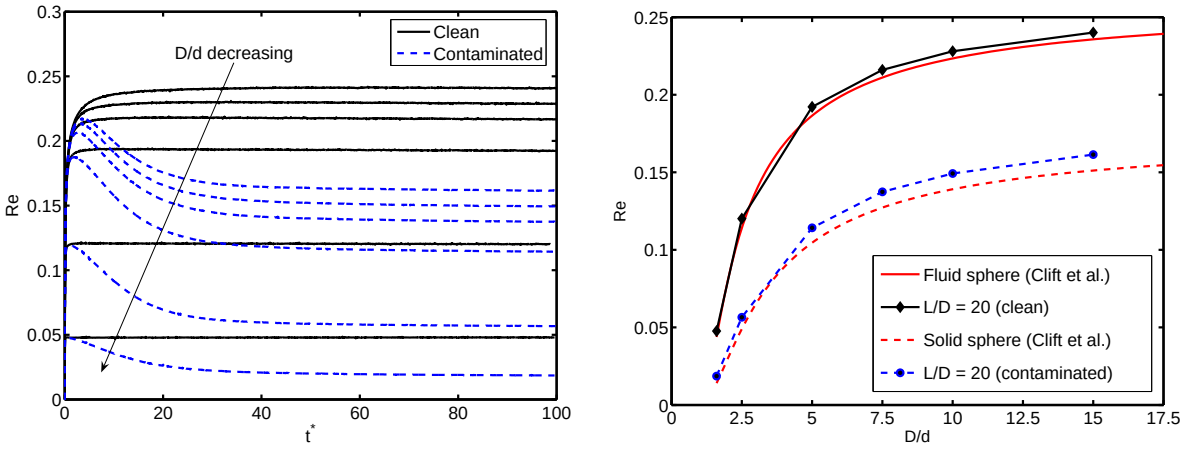


(a) (b)

Figure 4.1: Spherical bubble. (a) Reynolds number versus non-dimensional time for $D/d = 1.6, 2.5, 5, 7.5, 10$ and 15, and (b) steady Reynolds number versus non-dimensional channel diameter for clean (solid lines) and contaminated (dashed lines) bubbles ($Eo = 1$, $Mo = 0.1$).

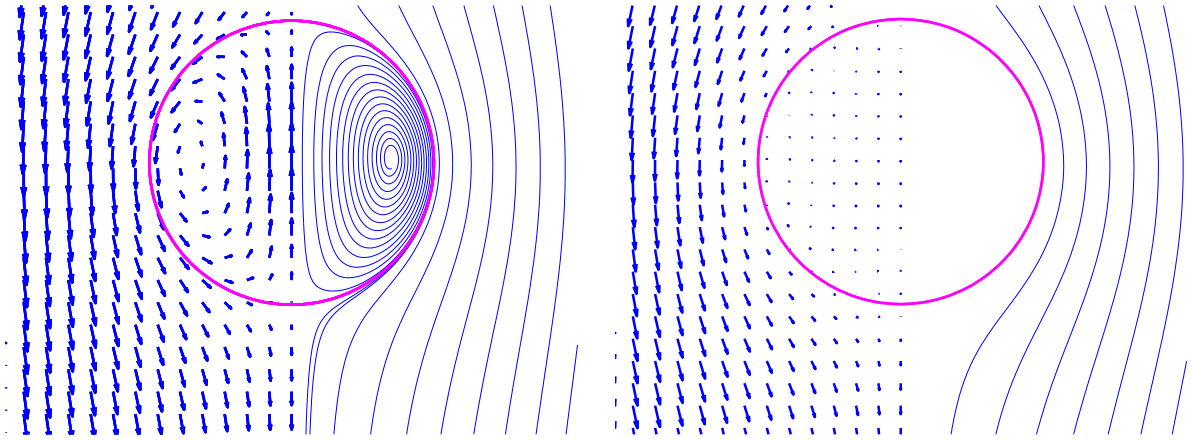

(a) (b)

Figure 4.2: Spherical bubble. The streamlines and the velocity vectors at steady-state in a coordinate system moving with the bubble centroid for (a) clean bubble (b) contaminated bubble. Every third grid points are used in the velocity vector plots ($Eo = 1$, $Mo = 0.1$).

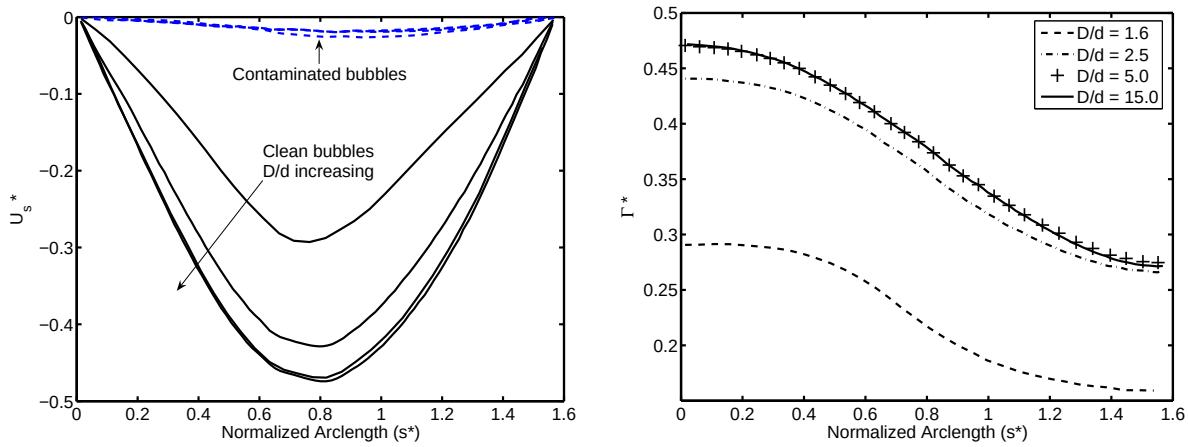


(a) (b)

Figure 4.3: Spherical bubble. (a) Surface velocity profiles of a clean (solid lines) and a contaminated (dashed lines) bubble and, (b) the interfacial surfactant concentration profiles for the channel diameters $D/d = 1.6, 2.5, 5$ and 15 at $t^* = 100$ ($Eo = 1, Mo = 0.1$).

and experimental results for the clean bubble case and the steady Reynolds number of the contaminated bubble approaches that of an equivalent solid sphere. The small discrepancy between the computed and experimental results for the clean bubble is partly attributed to the finite length of the periodic channel and the difference decreases as the channel length increases as discussed by Muradoglu and Tryggvason [36]. The flow fields are plotted in Fig. 4.2 both for the clean and contaminated bubbles rising in a large channel with $D = 15d$ and $L = 20d$ when bubbles reach a steady motion. A big vortex is created inside the clean bubble while the vortex inside the contaminated bubble nearly vanishes as it reaches a steady motion as depicted in Fig. 4.2b. This visually indicates the immobilization of the interface by the surfactant. The streamline patterns also change as the bubble gets contaminated. The spacing between streamlines is smaller when the bubble is clean and becomes larger as the bubble gets contaminated. The immobilizing effect of surfactant can be better seen from the surface velocities of the clean and contaminated bubbles plotted in Fig. 4.3a. In this figure, the non-dimensional surface velocities are plotted as a function of non-dimensional arc length measured from the centerline in the counter-clockwise direction for the non-dimensional channel diameters of $D/d = 1.6, 2.5, 5.0$ and 15.0 at $t^* = 100$. Figure 4.3a clearly shows that the non-dimensional steady surface velocity nearly vanishes

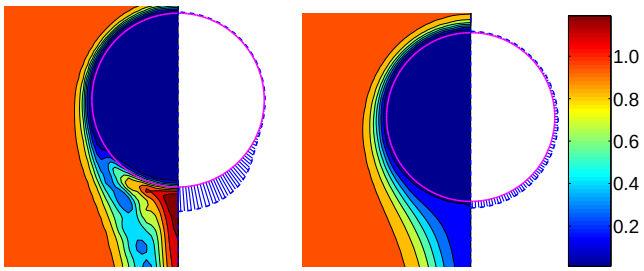


($\beta_s = 0.1$) ($\beta_s = 1.0$)

Figure 4.4: Spherical bubble. The contour plots of constant surfactant concentration in the bulk fluid (left side) and the distribution of the surfactant concentration at the interface (right side) with $\beta_s = 0.1$ (left plot) and $\beta_s = 1$ (right plot) at $t^* = 103.1$. Contour levels are the same in both cases ($Pe_c = 1000$, $Eo = 1$ and $Mo = 0.1$).

for the contaminated bubble case. On the other hand, the clean bubble surface has a significant velocity and it decreases while $D/d$ ratio decreases due to the increased wall effect. The wall effect is also apparent in distribution of interfacial surfactant concentration as seen in Fig. 4.3b where variation of interfacial surfactant concentration is plotted as a function of non-dimensional arc length. The wall has a considerable effect on the interfacial surfactant concentration when $D/d \leq 2.5$, and the wall effect reduces quickly and becomes negligible when $D/d \geq 5$.

### *4.1.2 The effect of the elasticity number*

Computations are performed to examine the effect of the elasticity number on the motion of a spherical bubble rising in a channel with $D = 5d$. For this purpose, the elasticity number is varied between $\beta_s = 0$ and $\beta_s = 1$, and $Pe_c = 1000$ while the other parameters are kept the same. Fig. 4.4 shows the bubble interface together with the contour plots of the constant surfactant concentration in the bulk fluid and the surfactant concentration distribution along the interface for $\beta_s = 0.1$ and 1 at $t^* = 103.1$.

The interfacial surfactant concentration becomes smoother as $\beta_s$ increases mainly due to reduced mobility of interface for larger values of $\beta_s$. Conversely, as $\beta_s$ decreases, the interface mobility increases so that the surfactant adsorbed at the leading edge of the bubble is convected quickly along the interface resulting in accumulation of surfactant at the back

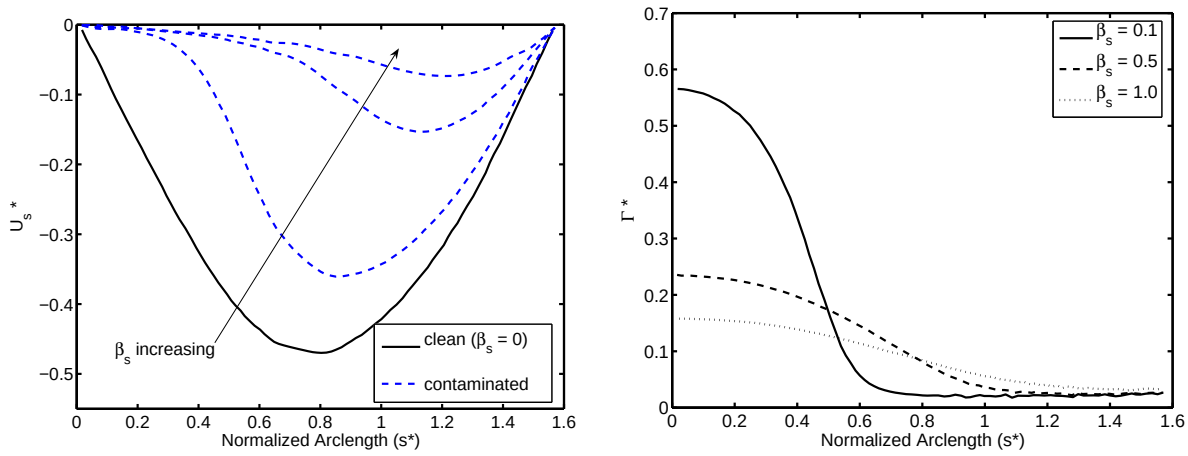


(a) (b)

Figure 4.5: Spherical bubble. (a)The surface velocity and (b) interfacial surfactant concentration as a function of arc length measured from the centerline in the counter-clockwise direction for $\beta_s = 0.1$, 0.5 and 1 at $t^* = 103.1$.

of the bubble. The effects of $\beta_s$ on the interface mobility and on the interfacial surfactant concentration distribution can be better seen in Fig. 4.5 where the non-dimensional surface velocity and interfacial surfactant concentration are plotted as a function of non-dimensional arc length for $\beta_s = 0.1$, 0.5 and 1 at $t^* = 103.1$. Here, as $\beta_s$ increases, interfacial surfactant concentration becomes more uniform and the magnitude of the surface velocity decreases significantly.

### *4.1.3 The effect of the bulk Peclet number*

For the spherical bubble case, we now examine the effect of the bulk Peclet number ($Pe_c$). For this purpose, $Pe_c$ is varied while the elasticity number is kept constant at $\beta_s = 0.5$. The contour plots of the constant bulk surfactant concentration and the surfactant concentration distribution at the interface are plotted in Fig. 4.6 for $Pe_c = 25$ and 1000 at $t^* = 103.1$. As shown in this figure, the surfactant concentration at the interface increases as $Pe_c$ decreases due to enhanced diffusivity of the surfactant in the ambient fluid. A thin boundary layer created on the bubble surface can also be seen from the counter levels of the bulk concentration for $Pe_c = 1000$. Fig. 4.7 shows the variation of non-dimensional surface

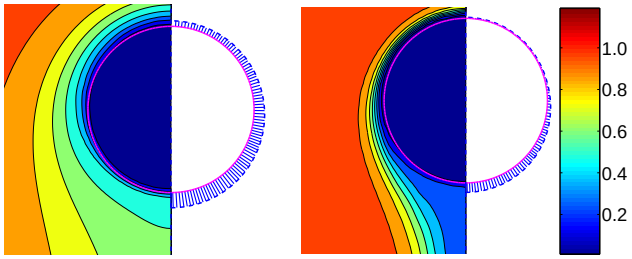


($Pe_c = 25$) ($Pe_c = 1000$)

Figure 4.6: Spherical bubble. The contour plots of constant surfactant concentration in the bulk fluid (left side) and the distribution of the surfactant concentration at the interface (right side) with $Pe_c = 25$ (left plot) and $Pe_c = 1000$ (right plot) at $t^* = 103.1$. Contour levels are the same in both cases ($\beta_s = 0.5, Eo = 1, Mo = 0.1$).

velocity and interfacial surfactant concentration as a function of non-dimensional arc length for $Pe_c = 25$, 100, 500 and 1000 at $t^* = 103.1$. It is clearly seen that, as $Pe_c$ decreases, the magnitude of the non-dimensional surface velocity diminishes while the interfacial surfactant concentration increases.

### *4.1.4 The effect of the Damkohler number*

In experiment, the bulk surfactant concentration is usually varied while the other parameters are kept constant. To mimic this, the Damkohler number is varied while keeping the other parameters the same as in Fig. 4.3 for a bubble rising in the channel with $D = 5d$ and $L = 20d$. In Fig. 4.8, the Reynolds number is plotted for various values of Damkohler number ranging between $Da = 1.25$ and $Da = 10$. As can be seen in this figure, the distance to reach a steady-state gets shorter as $Da$ decreases but the steady rise velocity seems to be independent of $Da$. This is qualitatively in a good agreement with the experimental observations of Zhang and Finch [10].

## *4.2 Ellipsoidal Case*

Next, we investigate effect of the soluble surfactants on the motion of a single bubble with significant deformation. We set $Eo = 10$ and $Mo = 0.001$ for which a clean bubble has an ellipsoidal shape in an unbounded domain as discussed by Clift et al. [1]. For this case, the

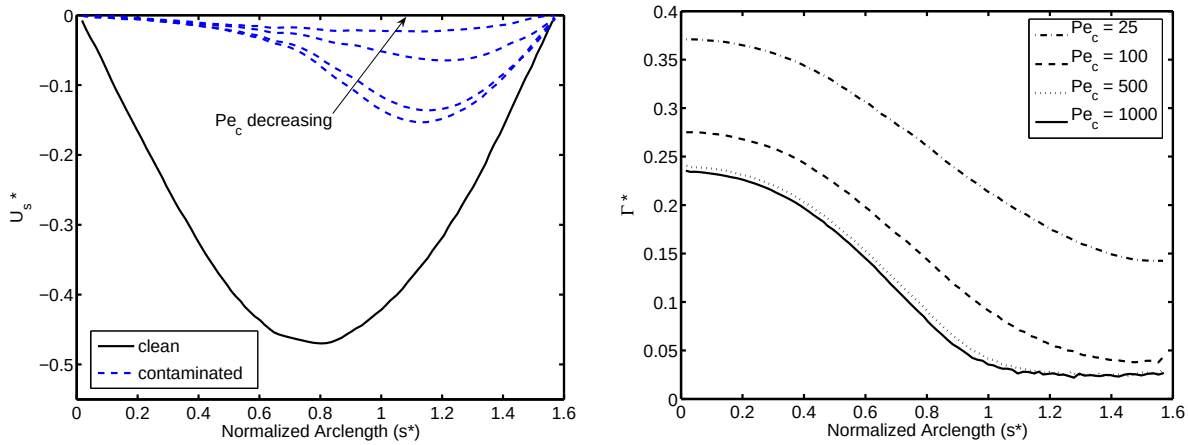


(a) (b)

Figure 4.7: Spherical bubble. (a) The surface velocity and (b) interfacial surfactant concentration as a function of arc length measured from the centerline in the counter-clockwise direction for $Pe_c = 25$, 100, 500 and 1000 at $t^* = 103.1$. ($Eo = 1$ and $Mo = 0.1$).

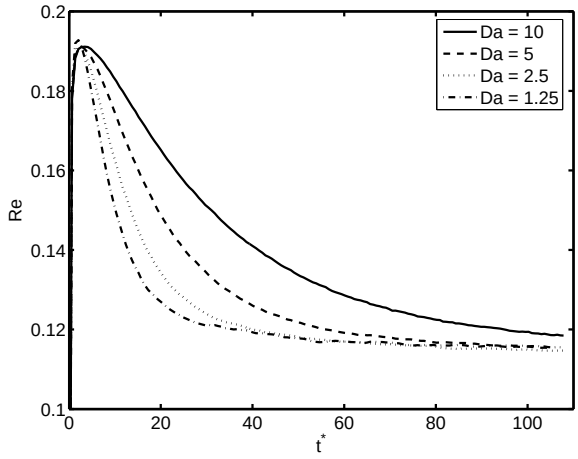


Figure 4.8: Spherical bubble. Reynolds number versus time for $Da = 10$, 5, 2.5 and 1.25 ($Eo = 1, Mo = 0.1$).

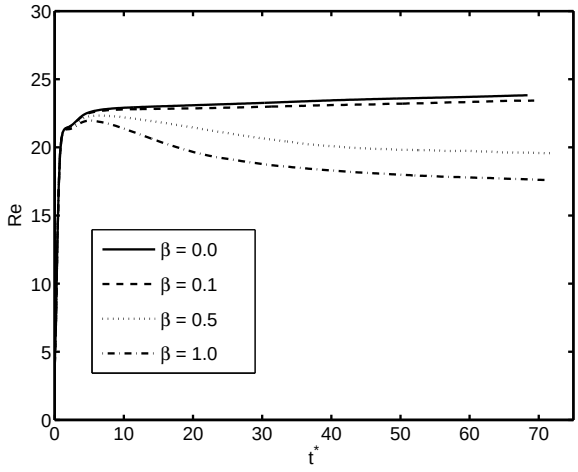


Figure 4.9: Ellipsoidal bubble. Reynolds number versus time for $\beta_s = 0.0$, 0.1, 0.5 and 1.0 ($Eo = 10, Mo = 0.001$).

channel size is $L = 50d$ in the axial direction and $D = 5d$ in the radial direction, and it is resolved by a $96 \times 1920$ uniform grid. The parameters are kept constant at $\rho_b/\rho_o = 0.1$, $\mu_b/\mu_o = 0.025$, $k = 1$, $Da = 10$ and $Bi = 0.75$.

### *4.2.1 The effect of the elasticity number*

First, effect of the elasticity number is examined. For this purpose, computations are performed for $\beta_s = 0$, 0.1, 0.25, 0.5 and 1 while keeping $Pe_c = 1000$ and $Pe_s = 100$. Fig. 4.9 illustrates the variation of Reynolds number as a function of the non-dimensional time for various elasticity values. As seen in this figure, terminal velocity decreases with increasing elasticity number but the reduction in the terminal velocity is not as dramatic as that observed in the spherical regime. Note that the computed Reynolds number of the clean bubble is 23.8 which is in a good agreement with the experimental value of 23.3, see for instance, Clift et al. [1]. The time evolutions of the surface velocity and interfacial surfactant concentration are plotted in Figs. 4.10a and 4.10b, respectively, for $\beta_s = 0.1$ and $\beta_s = 1$. The results are taken at $t^* = 9.7, 28.4, 48.4$ and 67.8. It is seen in Fig. 4.10a that the surface velocity does not change significantly in the case of $\beta_s = 0.1$ while its amplitude decreases quickly and the interface becomes nearly immobile in the case of $\beta_s = 1$ as bubble approaches a steady motion. The elasticity number also influences the interfacial surfactant

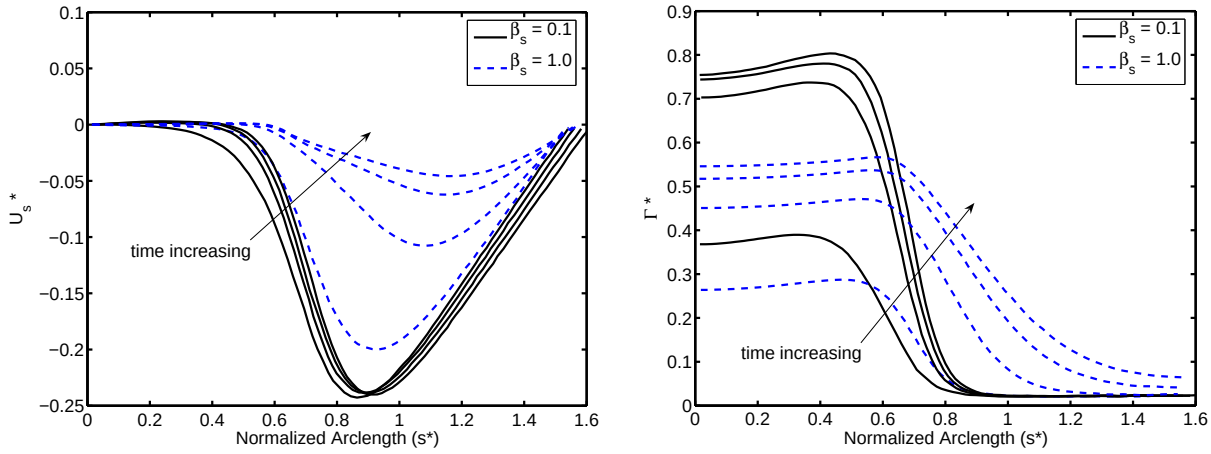


(a) (b)

Figure 4.10: Ellipsoidal bubble. (a) Surface velocity and (b) interfacial surfactant concentration versus arc length measured from the centerline in the counter-clockwise direction for $\beta_s = 0.1$ (solid lines) and $\beta_s = 1.0$ (dashed lines) at times $t^* = 9.7$, 28.4, 48.4, and 67.8 ($Eo = 10, Mo = 0.001$).

distribution as seen in Fig. 4.10b. In the case of small elasticity number ($\beta_s = 0.1$), the surfactant adsorbed at the leading edge of the bubble is swept quickly along the interface and accumulated at the back of the bubble due to the large surface mobility. The surfactant concentration is nearly flat at the back of the bubble and decreases rapidly at about $s^* = 0.6$, which is consistent with the stagnant-cap theory [1]. However, there is no discontinuity in the interfacial surfactant concentration partly due to diffusion along the interface and partly due to the Marangoni stresses acting in the opposite direction of the flow shear stress. In the case of large elasticity number ($\beta_s = 1$), the surfactant concentration is still flat at the back and it decreases at the front of the bubble. However, the distribution is more uniform and the transition is much smoother than the case of $\beta_s = 0.1$. The elasticity number also has a significant influence on the bubble deformation and on the overall flow structure as shown in Fig. 4.11 where the contours of constant bulk surfactant concentration are plotted together with the surfactant distribution at the interface in the top row, and the velocity vectors and streamlines are plotted in the vicinity of the bubble with respect to a coordinate system moving with the bubble centroid in the bottom row for $\beta_s = 0.1$, 0.25, 0.5 and 1. As seen, the surfactant adsorbed by the interface is swept back by the oncoming flow and accumulated

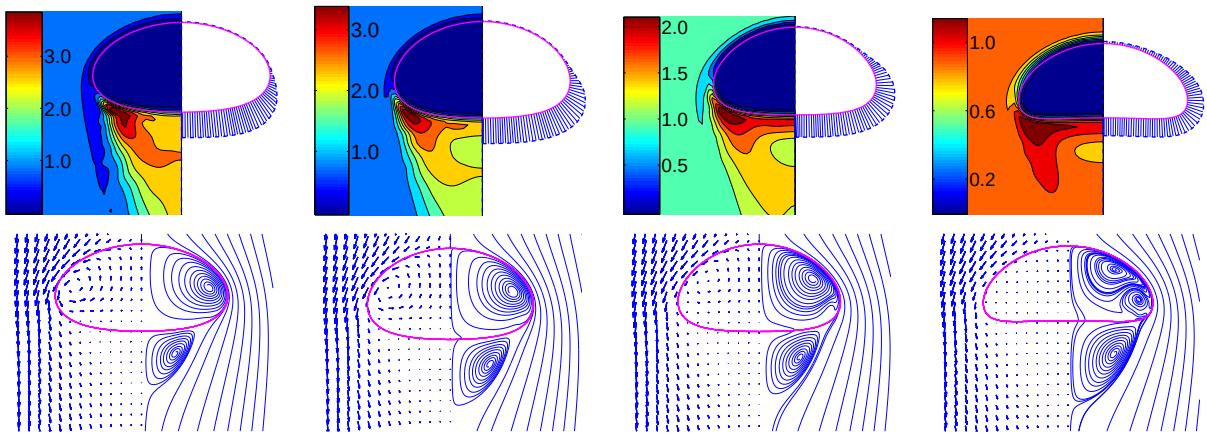


Figure 4.11: Ellipsoidal bubble. (Top row) The contour plots of the constant surfactant concentration in the bulk fluid (left side) and the distribution of the surfactant concentration at the interface (right side) with (from left to right) $\beta_s = 0.1$, 0.25, 0.5 and 1.0. (Bottom row) The streamlines and the velocity vectors in a coordinate system moving with the bubble centroid. Every third grid points are used in the vector plots ($Eo = 10, Mo = 0.001, Pe_c = 1000, Pe_s = 100, t^* = 67.8$).

there for all cases. However, the interfacial surfactant distribution gets more uniform as the elasticity number increases due to enhanced immobilizing effect of the surfactant at large $\beta_s$. As the surfactant is convected back along the interface and is accumulated at the back of the bubble, its concentration increases continuously and eventually exceeds the equilibrium interfacial concentration of the interface. After that the excessive surfactant is released into the bulk fluid and the interfacial surfactant concentration eventually becomes steady. This can be clearly seen from the contour plots of the bulk surfactant concentration in the top row of Fig. 4.11 and the time evolution of the interfacial surfactant concentration in Fig. 4.10b especially for the cases of small elasticity numbers, i.e., $\beta_s \leq 0.5$. The surfactant is mainly released from the interface into the bulk fluid near the stagnation points (e.g., at about $s^* = 0.6$ for this case) making the surfactant concentration relatively high in the bulk fluid there. The elasticity number also has a significant influence on the overall flow structure as seen in the velocity vectors and streamline plots in the bottom row of Fig. 4.11. For instance, while there is a big vortex created inside and a small recirculation region at the back of the bubble for small elasticity numbers (e.g., $\beta_s = 0.1$), the big vortex is broken

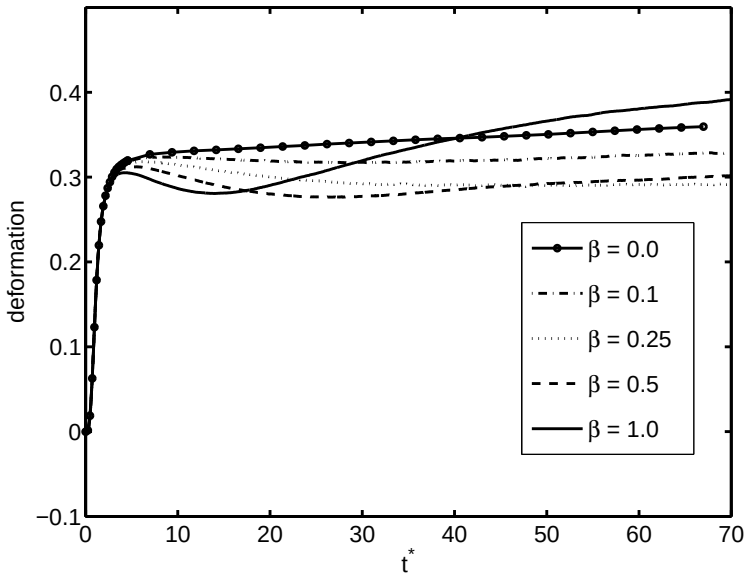


Figure 4.12: Ellipsoidal bubble. Effect of elasticity number on bubble deformation ($Eo = 10, Mo = 0.001, Pe_c = 1000, Pe_s = 100$).

into two smaller vortices and the recirculation region gets larger as the elasticity number is increased. It is also interesting to observe that, as the elasticity number increases, the bubble deformation first decreases due to rigidifying effect of the surfactants but it then increases due to overall reduction in surface tension. This can be better seen in Fig. 4.12 where the bubble deformation is plotted as a function of time for various values of $\beta_s$. Note that the deformation is defined as

$$\text{deformation} = \frac{W_b - H_b}{W_b + H_b}, \tag{4.2}$$

where $W_b$ and $H_b$ are the maximum bubble dimensions in the radial and axial directions, respectively. As can be seen in Figs. 4.11 and 4.12, bubble deformation is larger in the case of $\beta_s = 0.1$ than $\beta_s = 0.5$ case but smaller than $\beta_s = 1$ case. The surface velocity and the interfacial surfactant distribution are plotted in Figs. 4.13a and 4.13b, respectively, as a function of the arc length for various values of $\beta_s$. Similar to the spherical case, the surface mobility reduces significantly and the surfactant distribution becomes more uniform along the interface as $\beta_s$ increases.

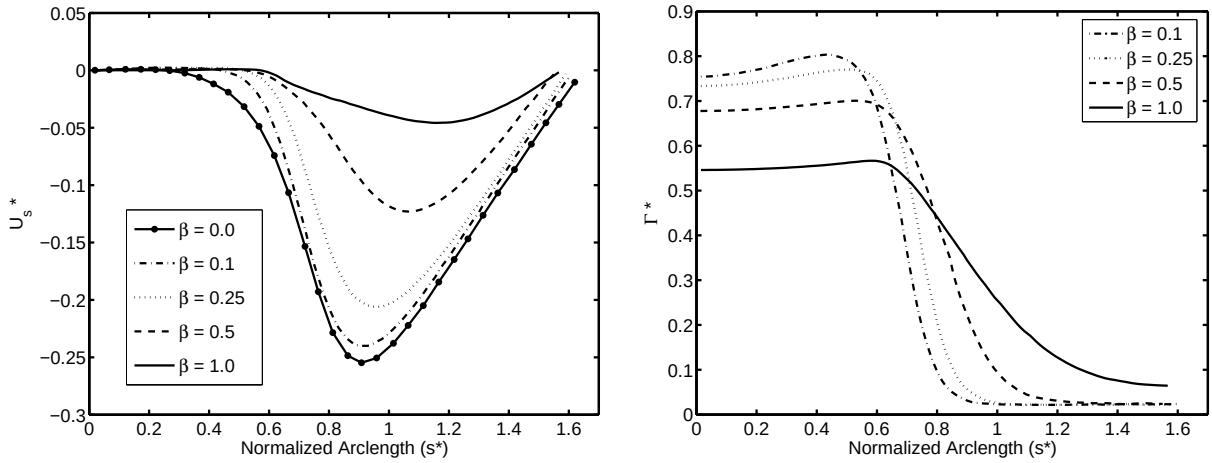


(a) (b)

Figure 4.13: Ellipsoidal bubble. (a) Surface velocity and (b) interfacial surfactant concentration as a function of non-dimensional arc length measured from the centerline in the counter-clockwise direction with $\beta_s = 0.1$, 0.25, 0.5 and 1.0 ($Eo = 10, Mo = 0.001, Pe_c = 1000, Pe_s = 100, t^* = 67.8$).

### *4.2.2 The effect of the bulk Peclet number*

The effect of the bulk Peclet number is also examined for the ellipsoidal regime. For this purpose, computations are performed for $Pe_c = 25$, 100, 500 and 1000 while keeping $Pe_s$ and $\beta_s$ fixed at 100 and 0.5, respectively. The time evolution of the surface velocity and distribution of the interfacial surfactant concentration are plotted in Figs. 4.14a and 4.14b, respectively, for $Pe_c = 25$ and $Pe_c = 1000$ cases. It can be seen from these figures that both the surface velocity and interfacial surfactant concentration reach steady state faster for $Pe_c = 25$ than for $Pe_c = 1000$ due to enhanced surfactant diffusion from bulk fluid to the bubble surface for small $Pe_c$. The constant contours of the bulk surfactant concentration and the interfacial surfactant concentration distributions are plotted in the top row of Fig. 4.15 at $t^* = 67.8$ while the velocity vectors and streamlines in the vicinity of the bubble are shown in the bottom row. We observe that $Pe_c$ does not have a big effect on the interfacial surfactant distribution and overall flow structure in the range between $Pe_c = 25$ and $Pe_c = 1000$. This can also be seen in the surface velocity and interfacial surfactant distribution plotted in Fig. 4.16. However it has stronger effect on the bulk surfactant concentration as the

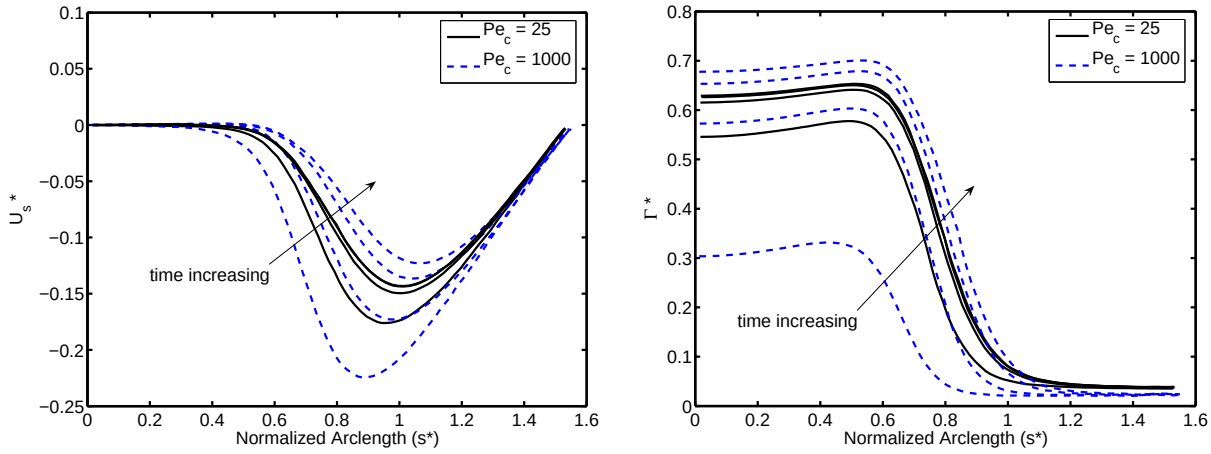


(a) (b)

Figure 4.14: Ellipsoidal bubble. (a) Surface velocity and (b) interfacial surfactant concentration as a function of arc length measured from the centerline in the counter-clockwise direction for $Pe_c = 25$ (solid lines) and $Pe_c = 1000$ (dashed lines) at times $t^* = 9.7$, 28.4, 48.4, and 67.8 ($Eo = 10, Mo = 0.001, \beta_s = 0.5, Pe_s = 100$).

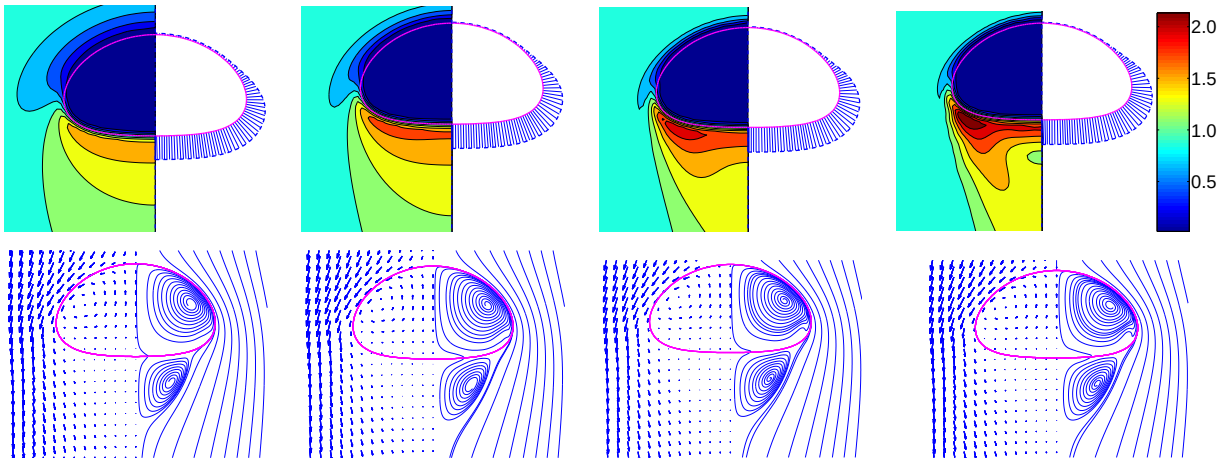

($Pe_c = 25$) ($Pe_c = 100$) ($Pe_c = 500$) ($Pe_c = 1000$)

Figure 4.15: Ellipsoidal bubble. (Top row) The contour plots of the constant surfactant concentration in the bulk fluid (left side) and the distribution of the surfactant concentration at the interface (right side) with (from left to right) $Pe_c = 25$, 100, 500 and 1000. (Bottom row) The velocity vectors and the streamlines in a coordinate system moving with the bubble centroid. Every third grid points are used in the vector plots ($Eo = 10, Mo = 0.001, \beta_s = 0.5, Pe_s = 100, t^* = 67.8$).

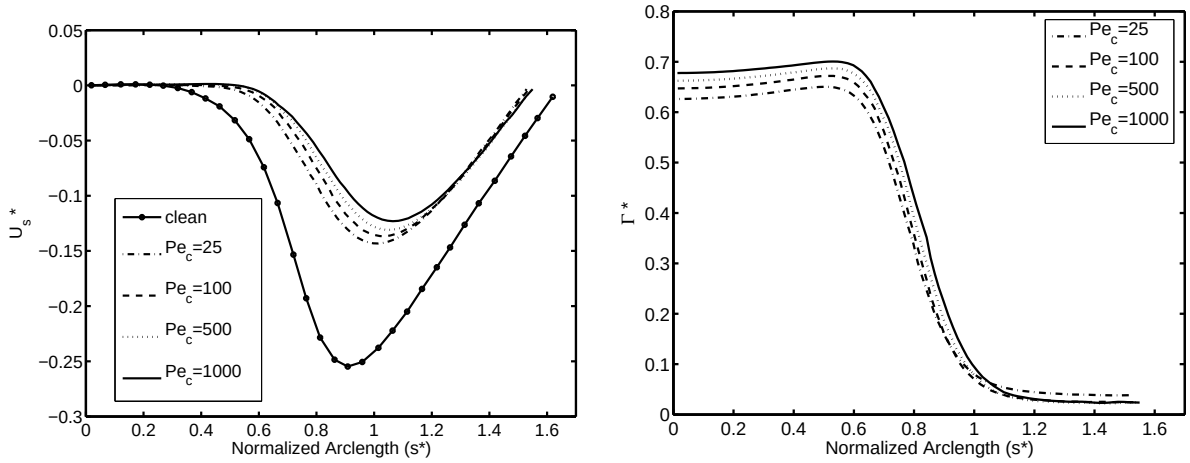


(a) (b)

Figure 4.16: Ellipsoidal bubble. (a) Surface velocity and (b) interfacial surfactant concentration as a function of arc length measured from the centerline in the counter-clockwise direction for $Pe_c = 25$, 100, 500 and 1000 ($Eo = 10, Mo = 0.001, \beta_s = 0.5, Pe_s = 100, t^* = 67.8$).

surfactant released from the interface near the stagnation point is quickly dissipated by the molecular diffusion making the bulk surfactant concentration more homogeneous in the recirculation region at the back of the bubble as $Pe_c$ gets smaller. In addition, the bulk surfactant concentration boundary layer at the leading edge of the bubble gets thinner as $Pe_c$ increases as can be seen from the contour plots in the top row of Fig. 4.15.

### *4.2.3 The effect of the interfacial Peclet number*

Finally, the effects of the interfacial Peclet number ($Pe_s$) are investigated for the ellipsoidal case by varying $Pe_s$ from 100 to $10^4$ while keeping $Pe_c$ and $\beta_s$ fixed at 1000 and 0.5, respectively. The contours of the constant bulk surfactant concentration and the distribution of the interfacial surfactant concentration are plotted in the top row of Fig. 4.17 while the velocity vectors and streamlines are depicted in the bottom row for various values of $Pe_s$. Figure 4.17 shows that $Pe_s$ generally has a significant influence on the bubble dynamics. The interface surfactant concentration becomes more uniform as $Pe_s$ decreases since surface diffusion counteracts the convection of the surfactant by the surface velocity. At high values of $Pe_s$, the surface diffusion becomes weak and the interfacial surfactant distribution

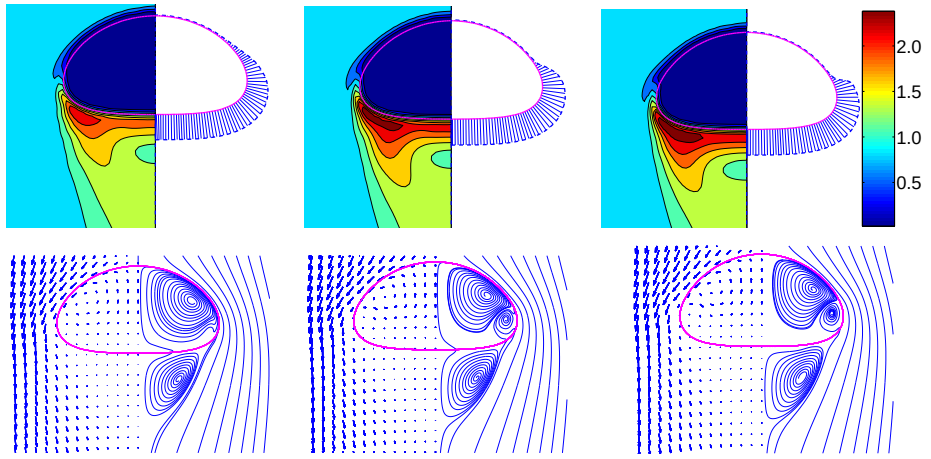


($Pe_s = 100$) ($Pe_s = 1000$) ($Pe_s = 10^4$)

Figure 4.17: Ellipsoidal bubble. (Top row) The contour plots of the constant surfactant concentration in the bulk fluid (left side) and the distribution of the surfactant concentration at the interface (right side) with (from left to right) $Pe_s = 100$, 1000 and $10^4$. (Bottom row) The velocity vectors and the streamlines in a coordinate system moving with the bubble centroid. Every third grid points are used in the vector plots ($Eo = 10, Mo = 0.001, Pe_c = 1000, \beta_s = 0.5, t^* = 67.8$).

approaches the stagnant-cap regime. In this regime, large concentration gradient induces large Marangoni stresses especially near the stagnation point and thus reduces the mobility of the interface. Similar to the large elasticity number cases, the big vortex inside the bubble is broken to create a smaller vortex after a critical value of $Pe_s$, i.e., about $Pe_s = 100$ in this case, and the smaller vortex gets larger when $Pe_s$ is increased beyond the critical value. In addition, the recirculation zone behind the bubble gets larger as $Pe_s$ increases. The effects of $Pe_s$ can also be seen in the surface velocity profiles and interfacial surfactant distributions plotted in Figs. 4.18a and 4.18b, respectively. The surface velocity continuously decreases while surfactant concentration becomes less uniform as $Pe_s$ increases until about $Pe_s = 1000$. After this point, $Pe_s$ does not have a significant influence on the surface mobility, interfacial surfactant distribution and the bubble motion in general.

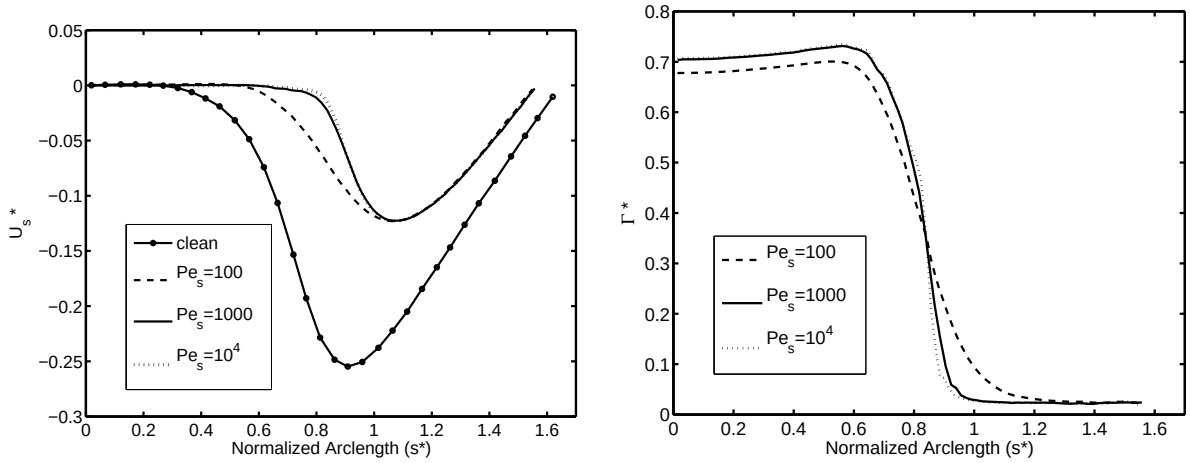


(a) (b)

Figure 4.18: Ellipsoidal bubble. (a) Surface velocity and (b) interfacial surfactant concentration as a function of arc length measured from the centerline in the counter-clockwise direction for $Pe_s = 100$, 1000 and $10^4$ ($Eo = 10, Mo = 0.001, \beta_s = 0.5, Pe_c = 1000, t^* = 67.8$).

### *4.3 Dimpled ellipsoidal-cap case*

Eötvös and Morton number are now set to 200 and 1000, respectively, for which a clean gas bubble takes a dimpled ellipsoidal-cap shape in an unbounded liquid in the steady motion [1]. The computations are performed both for clean and contaminated cases to show the effects of surfactants in this regime. However a parametric study is not repeated here and a simulation is performed for a single set of parameters by setting $Pe_c = 1000$, $Pe_s = 100$ and $\beta_s = 0.5$. The channel size is $D = 5d$ and $L = 20d$, and the computational domains of contaminated and clean cases are resolved by $256 \times 2048$ and $192 \times 1536$ uniform grids, respectively. Notice that the bubble is resolved by about 90 grid points in the axial direction for this case in order to better resolve the skirted rear part of the bubble. The constant contours of the bulk surfactant concentration together with the surfactant concentration distribution at the interface are plotted in Fig. 4.19a while the velocity vectors and streamlines are plotted for the contaminated and clean cases in Figs. 4.19b and 4.19c, respectively, at $t^* = 63.5$. The streamline and velocity vectors are again plotted with respect to a reference frame moving with the bubble centroid and every eighth grid points are used in the velocity vector plots. It is interesting to see that maximum interfacial surfactant concentration occurs at the back

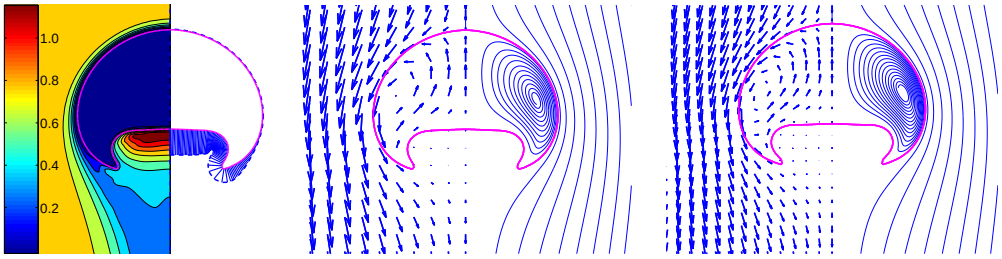


(a) (b) (c)

Figure 4.19: Dimpled ellipsoidal-cap. (a) The contour plots of the constant surfactant concentration in the bulk fluid (left side) and the distribution of the surfactant concentration at the interface (right side). The streamlines and the velocity vectors in a frame of reference moving with the bubble centroid for (b) a contaminated and (c) a clean bubble at $t^* = 63.5$. Every eighth grid points are used in the vector plots ($Eo = 200, Mo = 1000, Pe_c = 1000, Pe_s = 100, \beta_s = 0.5$).

of the bubble near the centerline and there is a high surfactant concentration region in the bulk fluid in the recirculation zone. The flow field seems not to be affected much by the surfactant except that the tip of the skirted rear part is slightly sharper in the contaminated case as can be seen in Figs. 4.19b and 4.19c. The surface velocity and interfacial surfactant concentration are plotted as a function of non-dimensional arc length in Figs. 4.20a and 4.20b, respectively, at times $t^* = 8.7$, 28.9, 46.2, and 63.5 to show the time evolution of these variables. The retardation effect of the surfactant is again seen in the surface velocity plot in this case but the effect is not as dramatic as that in the spherical bubble case. The surface velocity nearly vanishes in the wake region both in the clean and contaminated cases.

### *4.4 The effect of the Eötvös and Morton number*

Finally, the effects on the Eötvös number are studied by varying it from 0.1 to 30 while the other non-dimensional parameters are kept constant at $Pe_c = 100$, $Pe_s = 100$, $\beta_s = 1$, $D/d = 15$, $L/d = 30$, and $Mo = 0.001$. The steady Reynolds number is plotted in Figure 4.21a as a function of Eötvös number both for the clean and contaminated bubbles. As seen in this figure, the contamination significantly reduces the bubble terminal velocity at low Eötvös numbers, i.e., $Eo < 1$. However the terminal velocity of the contaminated

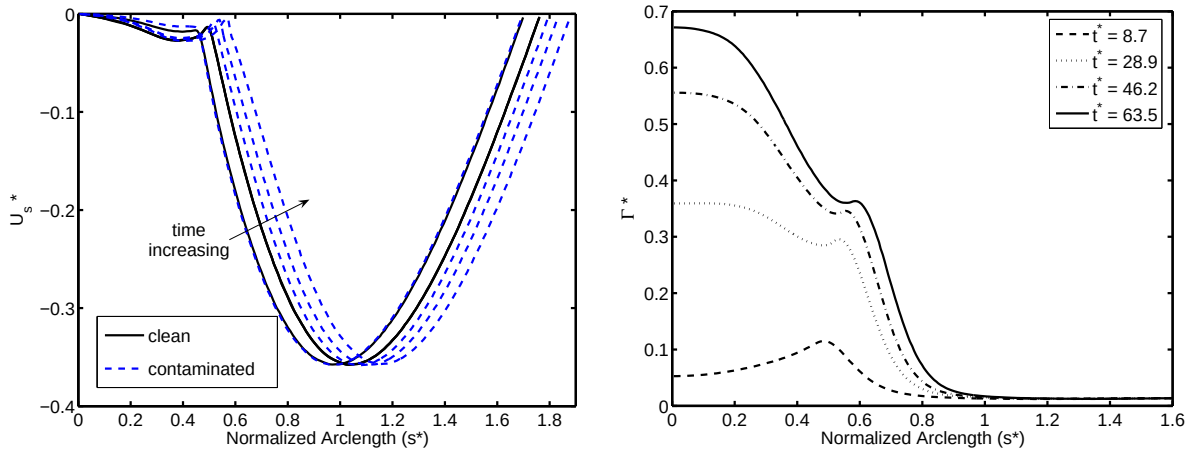


(a) (b)

Figure 4.20: Dimpled ellipsoidal-cap. (a) Surface velocity and (b) interfacial surfactant concentration as a function of arc length measured from the centerline in the counter-clockwise direction at times $t^* = 8.7$, 28.9, 46.2, and 63.5 ($Eo = 200, Mo = 1000, Pe_c = 1000, Pe_s = 100, \beta_s = 0.5$).

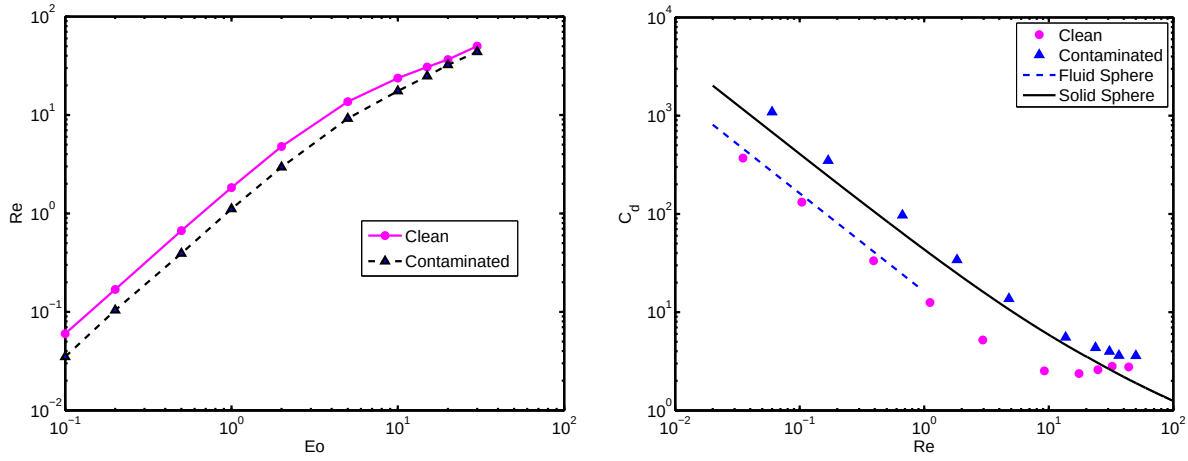


(a) (b)

Figure 4.21: Effects of the Eötvös number on the motion of the clean and contaminated bubbles. (a) The steady Reynolds number versus the Eötvös number. (b) The drag coefficient versus the Reynolds number.

bubble approaches that of the clean bubble for large Eötvös numbers, i.e., $Eo > 20$. The drag coefficient is another way to examine the effects of the contamination on the terminal velocity of the bubble. For a bubble, the drag coefficient is a function of the Reynolds, Eötvös and Morton numbers, and it can be deduced from the balance of forces acting on the bubble. In a steady motion of a bubble, when buoyancy force balances the drag force, the drag coefficient is given by [39]

$$C_d \equiv \frac{4}{3}\frac{\Delta\rho g d}{\rho_o V_b^2} = \frac{4}{3}\frac{Eo^{3/2}}{Re^2 Mo^{1/2}}, \tag{4.3}$$

where $V_b$ is the terminal velocity of the bubble. The drag coefficient is plotted in Fig. 4.21b as a function of the Reynolds number both for the clean and contaminated bubbles together with the experimental drag coefficients of fluid and solid spheres. The experimental correlations are plotted for the solid sphere when $Re \leq 100$ and for the fluid sphere when $Re \leq 1$ as recommended by Clift el al. [1]. As can be seen in this figure, the drag coefficient is slightly underpredicted for the clean bubble while it is overpredicted for the contaminated bubble. We observe that the drag coefficient of the clean bubble approaches to that of the contaminated bubble at large Reynolds numbers, i.e., $Re > 30$. However we have not observed in any case that the drag coefficient of the clean bubble exceeds that of the contaminated bubble, which is in contrast with the insoluble surfactant simulations of Jan [39].

# Chapter 5

# CONCLUSIONS

The effects of soluble surfactants on the motion and deformation of a gas bubble rising in an otherwise quiescent liquid contained in an axisymmetric channel are studied computationally using a finite-difference/front-tracking method. The Navier-Stokes equations are solved fully coupled with the bulk and interfacial surfactant concentration evolution equations and the surface tension is related to the interfacial surfactant concentration using a non-linear equation of state based on the Langmuir kinetics. The nearly spherical, ellipsoidal and dimpled ellipsoidal-cap regimes are considered and effects of governing nondimensional parameters including the elasticity number, the interfacial and bulk Peclet numbers and E*ö*tv*ö*s number are investigated.

It is found that the surfactants generally increase the drag force and thus reduce the terminal velocity of the bubble. However, the retardation effect of surfactants is stronger in the nearly spherical regime than the ellipsoidal and dimpled ellipsoidal-cap regimes. In this regime, the computations are performed to study the effects of confinement on the terminal velocity of the clean and contaminated bubbles. It is found that the computational results are in a very good agreement with the experimental correlations collected by Clift et al. [1] for the clean bubble and the steady terminal velocity of the contaminated bubble approaches that of an equivalent solid sphere. It is also found that the surface velocity of the contaminated bubble nearly vanishes and it behaves like a solid sphere when it reaches a steady motion. This rigidifying effect of the surfactant is also observed in the velocity vectors and streamline plots. The effects of the elasticity number and the bulk Peclet number are also examined in this regime. It is found that both parameters have significant influence on the bubble dynamics especially during its transient motion.

The effects of the nondimensional numbers on the bubble motion and deformation are examined more extensively in the ellipsoidal regime. It is found that $\beta_s$ and $Pe_s$ generally have a profound influence on the bubble dynamics. Both parameters significantly change

the surfactant concentration distribution on the interface and thus alter the overall flow structure. As $\beta_s$ increases, the surface velocity decreases significantly, the interfacial surfactant concentration becomes more uniform and the terminal velocity decreases. The bubble deformation first decreases with increasing $\beta_s$ due to increasing rigidity of the interface, i.e., until $\beta_s < 0.5$, but it starts increasing when $\beta_s$ is further increased due to overall reduction in surface tension. The flow structure is also affected significantly by $\beta_s$. A big vortex is created inside the bubble when $\beta_s$ is small, i.e., $\beta_s \leq 0.5$ and is broken into two smaller vortices when $\beta_s$ is increased beyond a critical value. In addition, the wake region behind the bubble gets larger as $\beta_s$ increases. $Pe_s$ also has significant influences on the bubble motion. The interfacial surfactant concentration becomes less uniform and, similar to $\beta_s$, the big vortex inside the bubble is broken into two smaller vortices and wake region is enlarged as $Pe_s$ is increased. We found that $Pe_c$ does not have a big influence on the bubble motion in the ellipsoidal regime in the range studied in this thesis, i.e., $25 \leq Pe_c \leq 1000$. Nevertheless the interfacial surfactant distribution increases slightly and thus the surface velocity is reduced as $Pe_c$ increases.

The retardation effect of the surfactant is also observed in the dimpled ellipsoidal regime but it is weaker than those in the spherical and ellipsoidal cases. The maximum interfacial surfactant concentration occurs at the back of the bubble near the axis of the symmetry. A high surfactant concentration core is created in the recirculation region in the bulk fluid and it sustains over the time due to continuous supply of surfactant released from the interface.

We also found that the drag coefficient of the clean bubble is slightly overpredicted compared to the experimental correlations while it is underpredicted for the contaminated bubble compared to the experimental data measured for an equivalent solid sphere. In addition, it is found that the drag coefficient of a clean bubble approaches that of the contaminated bubble at large Reynolds numbers, i.e., $Re > 30$.

# BIBLIOGRAPHY

[1] R. Clift, J.R. Grace and M.E. Weber, "Bubbles, drops and particles", *Dover*, Mineola, NY (2005).

[2] H.A. Stone, "Dynamics of drop deformation and breakup in viscous fluids", *Annu. Rev. Fluid Mech.*, Palo Alto, CA, **26**, 65 (1994).

[3] P. Duineveld, "The rise velocity and shape of bubbles in pure water at high Reynolds number", *Ph.D. Thesis*, Twente University, The Netherlands (1994).

[4] F. Takemura and A. Yabe, "Rising speed and dissolution rate of a carbon dioxide bubble in slightly contaminated water", *J. Fluid Mech.*, **378**, 319-334 (1999).

[5] J.S. Hadamard, *Compt. Rend.*, **152**, 1735 (1911).

[6] W. Rybczynski, *Bull. Int. Acad. Pol. Sci. Lett., Cl. Sci. Math. Nat., Ser. A*, 40 (1911).

[7] A.A. Frumkin and V.G. Levich, "On surfactants an interfacial motion, *Zhur. Fiz. Khim.*, **21**, 1183 (1947).

[8] Z. He, Z. Dagan and C. Maldarelli, "The influence of surfactant adsorption on the motion of a fluid sphere in a tube", *J. Fluid Mech.*, **222**, 1 (1991).

[9] R. Bel Fdliha and P. Duineveld, "The effect of surfactant on the rise of a spherical bubble at high Reynolds and Peclet numbers", *Phys. Fluids*, **8**, 310 (1996).

[10] Y. Zhang and J.A. Finch, "A note on single bubble motion in surfactant solutions", *J. Fluid Mech.*, **429**, 63 (2001).

[11] E. Almatroushi and A. Borhan, "Surfactant effect on the buoyancy-driven motion of bubble and drops in a tube", *Ann. N.Y. Acad. Sci.*, **1027**, 330 (2004).

[12] T. Yamaoto and T. Ishii, "Effect of surface active materials on the drag coefficient and shape of single large gas bubble", *Chem. Engng. Sci.*, **42**, 1297 (1987).

[13] P. Savic, "Circulation and distortion of liquid drops falling through a viscous medium", *Tech. Rep.*, MT-22, Natl. Res. Counc. Can., Div. Mech. Eng. (1953).

[14] R. Griffith, "The effect of surfactants on the terminal velocity of drops and bubbles", *Chem. Engng. Sci.*, **17**, 1057 (1962).

[15] J. Harper, "On spherical bubbles rising steadily in dilute surfactant solutions", *Q. J. Mech. Appl. Maths*, **27**, 87 (1974).

[16] J. Harper, "Surface activity and bubble motion", *Appl. Sci. Res.*, **38**, 343 (1982).

[17] J. Harper, "The leading edge of an oil slick, soap film, or bubble stagnant cap in Stokes flow", *J. Fluid Mech.*, **237**, 23 (1992).

[18] J. Harper, "Stagnant-cap bubbles with both diffusion and adsorption rate-determining", *J. Fluid Mech.*, **521**, 115-123 (2004).

[19] R. Davis and A. Acrivos, "The influence of surfactants on the creeping motion of bubbles", *Chem. Engng. Sci.*, **21**, 681 (1966).

[20] J. Holbrook and M. Levan, "The retardation of droplet motion by surfactant. Part 1. The theoretical development and asymtotic solutions", *Chem. Engng. Commun.*, **20**, 191 (1983).

[21] J. Holbrook and M. Levan, "The retardation of droplet motion by surfactant. Part 2. Numerical solutions for exterior diffusion, surface diffusion and adsorption kinetics", *Chem. Engng. Commun.*, **20**, 273 (1983).

[22] S. Sadhal and R. Johnson, "Stokes flow past bubbles and drops partially coated with thin films", *J. Fluid Mech.*, **126**, 237 (1983).

[23] Z. He, C. Maldarelli and Z. Dagan, "The size of stagnant caps of bulk soluble surfactant on the interfaces of translating fluid droplets", *J. Colloid Interface Sci.*, **146**, 442 (1991).

[24] D.M. Leppinen, M. Renksizbulut and R.J. Haywood, "The effects of surfactants on droplet behaviour at intermediate Reynolds numbers. I. The numerical model and steady-state results", *Chem. Engng. Sci.*, **51**, 491 (1996).

[25] D.M. Leppinen, M. Renksizbulut and R.J. Haywood, "The effects of surfactants on droplet behaviour at intermediate Reynolds numbers. II. Transient deformation and evaporation", *Chem. Engng. Sci.*, **51**, 491 (1996).

[26] J.B. McLaughlin, "Numerical simulation of bubble motion in water", *J. Coloid Interface Sci.*, **184**, 613-625 (1996).

[27] B. Cuenot, J. Magnaudet and B. Spennato, "The effects of slightly soluble surfactants on the flow around a spherical bubble", *J. Fluid Mech.*, **339** 25-53 (1997).

[28] F. Takemura, "Adsorption of surfactants onto the surface of a spherical rising bubble and its effect on the terminal velocity of the bubble", *Phys. Fluids*, **17**, 048104-048114 (2005).

[29] Y. Wang, D.T. Papageorgiou and C. Malderelli, "Increased mobility of a surfactant-retarded bubble at high bulk concentrations", *J. Fluid Mech.*, **390** 251-270 (1999).

[30] R. Palaparthi, D.T. Papageorgiou and C. Malderelli, "Theory and experiments on the stagnat cap regime in the motion of spherical surfactant-laden bubbles", *J. Fluid Mech.*, **559** 1-44 (2006).

[31] K. Sugiyama, S. Takagi and Y. Matsumoto, "Multi-scale analysis of bubbly flows", *Comput. Methods Appl. Mech. Engrg.*, **191**, 689-704 (2001).

[32] Y. Liao and J.B. McLaughlin, "Bubble motion in aqueous surfactant solutions", *J. Coloid Interface Sci.*, **224**, 297-310 (2000).

[33] X-J. Li and Z-S. Mao, "The Effect of Surfactant on the Motion of a Buoyancy-Driven Drop at Intermediate Reynolds Numbers: A Numerical Approach", *J. Coloid Interface Sci.*, **240**, 307-322 (2001).

[34] G. Ryskin and L.G. Leal, "Numerical solution of free-boundary problems in fluid mechanics. 1. The finite-difference technique", *J. Fluid Mech.*, **148**, 1-17 (1984).

[35] Y. Liao, J. Wang, R.J. Nunge and J.B. McLaughlin, "Comments on "Bubble motion in aqueous surfactant solutions"", *J. Coloid Interface Sci.*, **272**, 498-501 (2004).

[36] M. Muradoglu and G. Tryggvason "A Front-Tracking Method for Computation of Interfacial Flows with Soluble Surfactants", *J. Comp. Phys.*, **227**, 2238-2262 (2008).

[37] V.G. Levich, "Physicochemical Hydrodynamics", *Prentice Hall*, Upper Saddle River, NJ (1962).

[38] S.O. Unverdi and G. Tryggvason, "A front-tracking method for viscous incompressible multiphase flows", *J. Comput. Phys.*, **100**, 25 (1992).

[39] "Y.J. Jan, Computational studies of bubble dynamics", *Ph.D. Thesis*, The University of Michigan, Ann Arbor, MI (1994).

[40] H.A. Stone, "A simple derivation of the time-dependent convective-diffusion equation for surfactant transport along a deforming interface", *Phys. Fluids A*, **2**, 111 (1990).

[41] C.D. Eggleton and K.J. Stebe, "An adsorption-desorption controlled surfactant on a deforming droplet", *J. Coloid Interface Sci.*, **208**, 68-80 (1998).

[42] F.H. Harlow and J.E. Welch, "Numerical calculation of time-dependent viscous incompressible flow of fluid with free surface", *Phys. Fluids*, **8**, 2182 (1965).

[43] C. Peskin, "Numerical analysis of blood flow in the heart", *J. Comput. Phys.*, **25**, 220 (1977).

[44] J.C. Adams, "Mudpack: Multigrid Fortran software for the efficient solution of linear elliptical partial differential equations", *Appl. Math. Comput.*, **34**, 113 (1989).

[45] A.J. James and J. Lowengrup, "A surfactant-conserving volume-of-fluid method for interfacial flows with insoluble surfactants", *J. Comp. Phys.*, **201**, 685 (2004).

[46] G. Tryggvason, B. Bunner, A. Esmaeeli, D. Juric, N. Al-Rawahi, W. Tauber, J. Han, S. Nas and Y.-J. Jan, "A Front-Tracking Method for the Computations of Multiphase Flow", *J. Comput. Phys.*, **169(2)**, 708, (2001).

# VITA

SAVAS TASOGLU was born in Ankara, Turkey on November 28, 1983. He received his B.Sc. degree in Mechanical Engineering from Middle East Technical University, Ankara, in 2006. From August 2006 to August 2008, he worked as a teaching and research assistant with full TUBITAK scholarship in Koc University, Turkey. He published one peer-reviewed journal paper which featured the cover image of *Physics of Fluids*, April 2008. He studied about collision dynamics of fluid coated biological cells with a flat surface. Related papers were in preparation while thesis report was being prepared.